

# Transmitter-Side Voltage-Based Mutual Inductances and Load Tracking for Two-Transmitter *LCC-S* Compensated Wireless Power Transfer Systems

Kang Yue<sup>1</sup>, Graduate Student Member, IEEE, Yu Liu<sup>2</sup>, Senior Member, IEEE, Xinguo Zhang, Graduate Student Member, IEEE, Minfan Fu<sup>3</sup>, Senior Member, IEEE, Junrui Liang<sup>4</sup>, Senior Member, IEEE, and Haoyu Wang<sup>5</sup>, Senior Member, IEEE

**Abstract**—Tracking mutual inductances and load is essential for monitoring and control of wireless power transfer (WPT) systems. This article proposes an estimation method to identify the mutual inductances and load for a two-transmitter–one-receiver (2TX–1RX) *LCC-S* compensated WPT system. It only needs voltage measurements at the transmitter side, without requiring current sensors and information from the receiver side. This article first proposes a mathematical model that systematically describes the physical laws at the fundamental frequency and the third harmonic of the WPT system, where the rectifier and the load at the receiver side are equivalently modeled as a square wave source. This article also rigorously derives the reason why mutual inductances and load cannot be estimated simultaneously at the resonant frequency using a conventional equivalent resistor load model. In comparison, the proposed methodology ensures unique solutions of estimated parameters. Afterward, a state estimation method is applied to solve the unknown states of the system including mutual inductances and load information. Further controls such as maximum efficiency and constant output voltage/current controls can be implemented based on accurate tracking of system parameters using the transmitter-side information only. Hardware experiments on a prototype 2TX–1RX *LCC-S* WPT system validate the effectiveness of the proposed method.

**Index Terms**—Multitransmitter, mutual inductances and load tracking, parameter estimation, wireless power transfer (WPT).

Manuscript received 23 March 2023; revised 16 June 2023 and 17 August 2023; accepted 23 September 2023. Date of publication 16 October 2023; date of current version 4 April 2024. This work was supported in part by the National Natural Science Foundation of China under Grant 52377114; and in part by the Key Laboratory of Control of Power Transmission and Conversion, Ministry of Education, Shanghai Jiao Tong University (SJTU), under Grant 2022AB01. Recommended for publication by Associate Editor Chi Kwan Lee. (Corresponding author: Yu Liu.)

Kang Yue is with the Shanghai Advanced Research Institute, Chinese Academy of Sciences, Shanghai 201210, China, also with the University of Chinese Academy of Sciences, Beijing 101408, China, and also with the School of Information Science and Technology, Shanghai 201210, China.

Yu Liu is with the Key Laboratory of Control of Power Transmission and Conversion, Ministry of Education, Shanghai Jiao Tong University (SJTU), Shanghai 200240, China, and also with the School of Information Science and Technology, Shanghai 201210, China (e-mail: liuyu.shanghaitech@gmail.com; liuyu@shanghaitech.edu.cn).

Xinguo Zhang, Minfan Fu, Junrui Liang, and Haoyu Wang are with the School of Information Science and Technology, Shanghai 201210, China.

Color versions of one or more figures in this article are available at <https://doi.org/10.1109/JESTPE.2023.3324792>.

Digital Object Identifier 10.1109/JESTPE.2023.3324792

## I. INTRODUCTION

WIRELESS power transfer (WPT) systems are widely adopted in many charging applications, such as electrical vehicles (EV), portable devices, and implantable biomedical devices [1], [2], [3], [4], [5]. Wireless charging with no cables and plugs brings safety and convenience for the applications. The inductive WPT systems deliver power from transmitting (TX)-to-receiving (RX) coils based on the electromagnetic induction. The WPT systems should usually realize specific control objectives, such as constant voltage output, constant current (CC) output, and maximum efficiency. In many inductive charging scenarios, coil misalignment will cause changes in mutual inductances [6]; the loads are also not constant [7]. Accurate knowledge of the mutual inductances and load is essential to realize the aforementioned control objectives [8], [9], [10]. Therefore, researchers proposed various parameter estimation methods. This article first reviews parameter estimation methods for 1TX–1RX WPT systems, and then introduces specific considerations for multicoil WPT systems.

For conventional 1TX–1RX WPT systems, wireless communication is one intuitive way to transfer information from the receiver to the transmitter. With these communication methods, the output voltage/current and the load at the receiver side can be obtained directly, which simplifies the problem of parameter identification. However, these methods require sensors and wireless communication circuits implemented on both sides, increasing the cost and complexity of the system. In addition, wireless signals could be susceptible to electromagnetic interference [11], [43].

To overcome the above challenges caused by wireless communication, many researchers studied the parameter identification methods that only utilize the measurements (voltage, current, and duty cycle) from the transmitter side to estimate the mutual inductances and loads, avoiding communication with receiver side and reducing hardware costs [12], [13], [14], [15], [16], [17], [18], [19], [20], [21], [22], [23]. In [12], [13], [14], and [15], the mutual inductance is estimated with the relationship between the input impedance and the mutual inductance. Hu et al. [14] simplified the circuit model based on high-frequency harmonic characteristics of the resonator

to improve the accuracy. These methods assume known load parameters and only estimate the mutual inductance. Sheng and Shi [16], Su et al. [17], [18], Yin et al. [19], Liu et al. [20], Dai et al. [21], Yang et al. [22], and Chow et al. [23] estimate both the mutual inductance and load simultaneously with the transmitter-side information. These methods usually apply the equivalent circuit model of the WPT system and analyze the input impedance of the system by measuring the transmitter-side voltage, current or the phase shift between the voltage and current. The key point is to generate sets of equations demonstrating the relationship among states and input impedance of the equivalent circuit model, and then obtain the states by solving the equations. Sheng and Shi [16] and Su et al. [17] add auxiliary circuits (inverters or compensated capacitors) to generate discrete operating modes and further obtain more information (sets of different steady-state equations). Additional circuits or components may increase the control complexity and cost of the system. Moreover, switching between various modes may affect the operating conditions and transfer efficiency. With no additional circuits, Su et al. [18] obtain two sets of analytical solutions of the parameters by building the ac impedance model for secondary parallel-compensated WPT systems. Then, it eliminates the undesired solutions with the analysis of the range of parameters. Yin et al. [19] give the mathematical expression of mutual inductance and load at any operating frequency except the resonant frequency of the receiver circuit in series-series (SS) compensated systems. Liu et al. [20], Dai et al. [21], and Yang et al. [22] generate the input impedance equations in discrete frequency/harmonic frequency to solve the parameters for the receiver series-compensated WPT system. Chow et al. [23] generate the equations for SS compensated system and obtain the mutual inductance within a reasonable range. For these studies, it is reported that for receiver series-compensated WPT systems, infinite-solution issues typically occur at the resonant frequency for the estimation of mutual inductance and load [19].

The 1TX-1RX WPT systems could suffer from coil misalignment and weak coupling. Hence, multi-TX WPT systems are developed to expand the charging area and improve the coupling [24], [25], [26], [28], [29], [30]. Application examples include the charging of electric vehicles [44], [45], and improvement of charging flexibility with omnidirectional charging [46], [47], [48], among others. Similar to 1TX-1RX WPT system, maximum efficiency and proper output controls are significant objectives for multi-TX WPT, where mutual inductances and load identification are also of great importance. Compared with one-TX systems, there are additional challenges for mutual inductances and load tracking for multi-TX systems. The physical laws of multi-TX systems are more complex, and more parameters need to be estimated, such as mutual inductances between each TX coil and the receiving (RX) coil. To meet the challenges, a limited number of the literature studied the parameters identification method for multi-TX WPT systems. Huh and Ahn [25], Kim et al. [26], and Kim and Ahn [27] achieve the maximum efficiency of the two-TX WPT system by tuning the input current of the transmitter according to mutual inductances. Different from

one-TX systems, only the receiver-side information (voltage and load) cannot uniquely determine the mutual inductance, Kim et al. [26] derive the additional mutual inductance ratio based on input impedance to solve the parameters. Dai et al. [28], [29] derive the relation among the input current, voltage, and reflection impedance at the resonant frequency for multi-TX WPT systems. It measures the load value and uses communication to outline mutual inductances and to avoid infinite-solution problems. Li et al. [30] estimate the mutual inductance and load for dual-LCC WPT systems based on impedance analysis, solving the infinite-solution problem by tuning the LCC parameters. These studies show that compared with SS topology, the LCC-S topology can be applied in multi-TX WPT systems with higher design freedom and less current stress [29]. From these studies, methods for estimating parameters in multi-TX WPT systems also encounter challenges as follows: 1) most methods only estimate the mutual inductances, and fail to estimate mutual inductances and load simultaneously; 2) most methods model the load as an equivalent resistor; infinite-solution problems typically exist for mutual inductance estimation, and the reason still needs to be systematically investigated; and 3) receiver-side information and wireless communication are typically required, increasing the cost and complexity of the system.

High-order harmonics are widely utilized to identify the parameters in the area of power systems, power electronics, and electric machinery [31], [32], [33], [34], [35], providing more information for the parameter identification problem. In this article, the high-order harmonics are considered for mutual inductances and load tracking in a two-transmitter-one-receiver (2TX-1RX) LCC-S WPT system. It estimates the mutual inductances and load simultaneously using the transmitter-side information only. The method first builds an equivalent circuit model of the system including the mutual inductances and the output voltages/currents as independent states. Fundamental and high-order harmonic components are taken into consideration during the modeling. This modeling methodology systematically avoids the issues of infinite solutions. Afterward, the state estimation method is applied to solve the states of the system, including mutual inductances and load information. With the estimated states, further control strategies can be implemented without the remote side information. The key contributions of the proposed mutual inductances and load tracking method are summarized as follows.

- 1) For 2TX-1RX LCC-S WPT systems, this article systematically investigates the reason for infinite solutions of parameters at the resonant frequency (dependency among parameters) using an equivalent resistor load model, with rigorous mathematical proofs.
- 2) A modeling method using harmonics for 2TX-1RX LCC-S WPT system is presented, to avoid the parameter dependency problem; the proposed framework can estimate mutual inductances and load information simultaneously with unique solutions.
- 3) The proposed estimation method has no assumption of the operating frequency of the system and can work at the resonant frequency; it only needs to measure

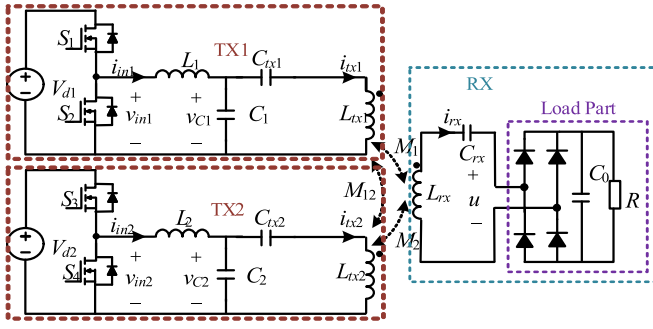


Fig. 1. 2TX-1RX LCC-S compensated WPT system.

transmitter side voltages; no current sensor, addition circuit, or communication channel is needed.

- 4) With the estimated parameters, control strategies to achieve the maximum transfer efficiency and constant output voltages/currents can be implemented without requiring any feedback signal from the receiver side.

The rest of this article is arranged as follows. Section II presents the conventional and the proposed modeling procedure of a 2TX-1RX LCC-S WPT system, with rigorous mathematical derivations and proofs. Section III introduces the estimation procedure based on the state estimation method. Section IV introduces the possible applications with the estimated mutual inductances and load, such as maximum efficiency control and constant output voltage/current control. Section V shows the hardware experimental results to verify the effectiveness of the proposed estimation method and control applications. Section VI makes further discussions. Section VII provides the conclusion of this article.

## II. PROPOSED MODELING METHODOLOGY

Typical WPT systems consist of dc power supplies, inverter circuits, compensation circuits, TX and RX coils, rectifier circuits and loads. Fig. 1 shows a typical multi-coil LCC-S WPT system, containing two transmitters and one receiver. The two transmitters have the same compensation topology.  $L_1$ ,  $C_1$ , and  $C_{tx1}$ , and  $L_2$ ,  $C_2$ , and  $C_{tx2}$  are the LCC compensation components for the TX coils  $L_{tx1}$  and  $L_{tx2}$ , respectively. The two TX coils  $L_{tx1}$  and  $L_{tx2}$  are both coupled with the RX coil  $L_{rx}$ .  $C_{rx}$  is the compensated component of the RX coil  $L_{rx}$ .  $M_1$  and  $M_2$  are the mutual inductances between each TX coil and the RX coil, respectively.  $M_{12}$  is the mutual inductance between the two TX coils.

Modeling the WPT system is to find the voltage/current relationship to describe the physical laws of the system. The modeling procedure can be divided into two parts: one is to model the transmitter side circuit, and the other is to model the receiver side circuit including the rectifier circuit and the load resistor. Therefore, this section first introduces the modeling method for the transmitter side in Section II-A. Afterward, modeling methods for the receiver side with different load part equivalence are shown in Section II-B, with the load part modeled as an equivalent resistor or an equivalent square wave source.

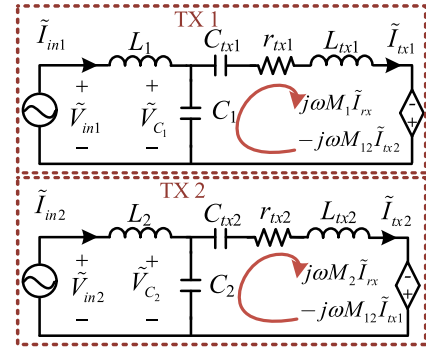


Fig. 2. Equivalent circuit of the transmitter-side circuit.

### A. Modeling Transmitter-Side Circuit

For the WPT system shown in Fig. 1, the equivalent circuit of the transmitter side is shown in Fig. 2.

$\tilde{V}_{in1}$  and  $\tilde{V}_{in2}$  are the output voltages of the inverter, which are modeled as square wave sources containing the fundamental frequency and multiple harmonic components.  $\tilde{V}_{C1}$  and  $\tilde{V}_{C2}$  are the voltages across  $C_1$  and  $C_2$ , respectively.  $\tilde{I}_{tx1}$  and  $\tilde{I}_{tx2}$  are the currents through the two TX coils, respectively. For the  $n$ th harmonic component (including the fundamental frequency component where  $n = 1$ ), one can demonstrate the transmitter side model as (1) based on the KVLs within the right side meshes (as shown in the figure)

$$\begin{aligned} \tilde{V}_{C1,n} &= \tilde{I}_{tx1,n} Z_{1,n} - j\omega_s M_1 \tilde{I}_{rx,n} + j\omega_s M_{12} \tilde{I}_{tx2,n} \\ \tilde{V}_{C2,n} &= \tilde{I}_{tx2,n} Z_{2,n} - j\omega_s M_2 \tilde{I}_{rx,n} + j\omega_s M_{12} \tilde{I}_{tx1,n} \end{aligned} \quad (1)$$

where the impedances are  $Z_{1,n} = j\omega_s L_{tx1} - j/(\omega_s C_{tx1}) + r_{tx1}$  and  $Z_{2,n} = j\omega_s L_{tx2} - j/(\omega_s C_{tx2}) + r_{tx2}$ .  $r_{tx1}$  and  $r_{tx2}$  are the equivalent series resistances (ESRs) of the TX coils TX1 and TX2, respectively. The signal  $(\cdot)_n$  represents the  $n$ th harmonic component of the variable  $(\cdot)$ .  $\omega_s$  is the angular frequency of the waveform  $\tilde{V}_{in1}$  and  $\tilde{V}_{in2}$ , i.e., the angular switching frequency of S1-S4. It should be noted that the equation set in (1) describes the  $n$ th harmonic model of the system, where  $n$  can be selected as a positive integer. Obtaining discrete harmonic frequency components of the system can provide more information and improve the system redundancy for the estimation problem.

In fact, since the estimation problem is only based on the transmitter side information, the unknown voltages and currents in (1) that could be measured include  $\tilde{V}_{C1}$ ,  $\tilde{V}_{C2}$ ,  $\tilde{I}_{tx1}$ , and  $\tilde{I}_{tx2}$ . However, the hardware of current measurements is more complicated and challenging than that of voltage measurements. In this article, the current measurements  $\tilde{I}_{tx1}$  and  $\tilde{I}_{tx2}$  can be calculated by the voltage measurements  $\tilde{V}_{C1}$  and  $\tilde{V}_{C2}$  as well as the source voltages  $\tilde{V}_{in1}$  and  $\tilde{V}_{in2}$ , as shown in (2). In this case, only the voltage measurements are required

$$\begin{aligned} \tilde{I}_{tx1,n} &= \tilde{V}_{in1,n}/(j\omega_s L_1) + j(1/(\omega_s L_1) - \omega_s C_1)\tilde{V}_{C1,n} \\ \tilde{I}_{tx2,n} &= \tilde{V}_{in2,n}/(j\omega_s L_2) + j(1/(\omega_s L_2) - \omega_s C_2)\tilde{V}_{C2,n}. \end{aligned} \quad (2)$$

### B. Modeling Receiver-Side Circuit

The equivalent circuit of the receiver side is shown in Fig. 3.  $r_{rx}$  is the ESR of the RX coil. Specifically, to represent the load

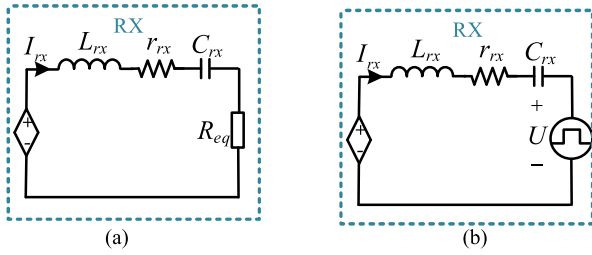


Fig. 3. Equivalent circuit of the receiver side. (a) Equivalent resistor model. (b) Equivalent square wave source model.

part (including the rectifier, capacitor  $C_0$ , and load  $R$ , as shown in Fig. 1), Fig. 3(a) utilizes an equivalent resistor model, while Fig. 3(b) adopts an equivalent square wave source model.

1) *Modeling Method 1 (Equivalent Resistor Model)*: To simplify the analysis of the WPT system, many existing literature adopt the equivalent resistor model. The load part is modeled as a pure ac resistance  $R_{eq} = 8R/\pi^2$  [11], [12], [13], [14], [15], [16], [17], [18], [19], as shown in Fig. 3(a). Note that this equivalence only holds for the fundamental frequency since  $R_{eq}$  is calculated via power equivalencing at the fundamental frequency. The model is

$$0 = j\omega_s M_1 \tilde{I}_{tx1,1} + j\omega_s M_2 \tilde{I}_{tx2,1} - \tilde{I}_{rx,1} (Z_{r,1} + R_{eq}) \quad (3)$$

where  $Z_{r,1} = j\omega_s L_{rx} - j/(\omega_s C_{rx}) + r_{rx}$  is the fundamental frequency series impedance at the receiver side excluding the equivalent load  $R_{eq}$ .

With the transmitter-side model (1) and the equivalent resistor model at the fundamental frequency ( $n = 1$ ) in (3), the overall model of the system is

$$\begin{aligned} \tilde{V}_{C1,1} &= \tilde{I}_{tx1,1} Z_{1,1} - j\omega_s M_1 \tilde{I}_{rx,1} + j\omega_s M_{12} \tilde{I}_{tx2,1} \\ \tilde{V}_{C2,1} &= \tilde{I}_{tx2,1} Z_{2,1} - j\omega_s M_2 \tilde{I}_{rx,1} + j\omega_s M_{12} \tilde{I}_{tx1,1} \\ 0 &= j\omega_s M_1 \tilde{I}_{tx1,1} + j\omega_s M_2 \tilde{I}_{tx2,1} - \tilde{I}_{rx,1} (Z_{r,1} + R_{eq}). \end{aligned} \quad (4)$$

In (4), there are three complex equations.  $\tilde{V}_{C1,1}$ ,  $\tilde{I}_{tx1,1}$ ,  $\tilde{V}_{C2,1}$ , and  $\tilde{I}_{tx2,1}$  and  $\omega_s$ ,  $Z_{2,1}$ ,  $Z_{1,1}$ , and  $Z_{r,1}$  are the known measurements and parameters, respectively. By separating (4) into real and imaginary parts, the model has six real equations and six real unknown states:  $\tilde{I}_{rx,1}$  is a complex variable consisting of two real unknowns, and  $M_1$ ,  $M_2$ ,  $M_{12}$ , and  $R_{eq}$  are the four unknown real variables. At first glance, it seems that the redundancy of the system is enough, and the unknown variables can be solved. However, the unknowns cannot be solved if the system operates at the resonant frequency due to the dependency among those unknowns. Next, the reason is explained in detail.

2) *Parameter Dependency at Resonant Frequency Using Modeling Method 1*: For WPT systems with the example LCC-S topology, the relationships between inductors and capacitors within the circuit are shown in the following equation, where  $\omega_0$  is the resonant frequency

$$\begin{aligned} \omega_0 &= 1/\sqrt{L_1 C_1} & \omega_0 &= 1/\sqrt{(L_{tx1} - L_1) C_{tx1}} \\ \omega_0 &= 1/\sqrt{L_{rx} C_{rx}} & \omega_0 &= 1/\sqrt{L_2 C_2} \\ \omega_0 &= 1/\sqrt{(L_{tx2} - L_2) C_{tx2}}. \end{aligned} \quad (5)$$

For the system operating at  $\omega_0$ ,  $\omega_s = \omega_0$ . With (5), the impedances can be expressed as  $Z_{r,1} = r_{rx}$ ,  $Z_{1,1} = j\omega_0 L_1 + r_{tx1}$ , and  $Z_{2,1} = j\omega_0 L_2 + r_{tx2}$ . From the last row of (4),  $\tilde{I}_{rx,1} = (j\omega_0 M_1 \tilde{I}_{tx1,1} + j\omega_0 M_2 \tilde{I}_{tx2,1}) / (r_{rx} + R_{eq})$ . Substitute  $\tilde{I}_{rx,1}$  into the first two rows of (4)

$$\begin{aligned} \tilde{V}_{C1,1} &= \tilde{I}_{tx1,1} \left( j\omega_0 L_1 + r_{tx1} + \frac{\omega_0^2 M_1^2}{r_{rx} + R_{eq}} \right) \\ &\quad + \tilde{I}_{tx2,1} \left( \frac{\omega_0^2 M_1 M_2}{r_{rx} + R_{eq}} + j\omega_0 M_{12} \right) \\ \tilde{V}_{C2,1} &= \tilde{I}_{tx2,1} \left( j\omega_0 L_2 + r_{tx2} + \frac{\omega_0^2 M_2^2}{r_{rx} + R_{eq}} \right) \\ &\quad + \tilde{I}_{tx1,1} \left( \frac{\omega_0^2 M_1 M_2}{r_{rx} + R_{eq}} + j\omega_0 M_{12} \right). \end{aligned} \quad (6)$$

In (6), the mutual inductance  $M_1$  or  $M_2$  always appears together with the term  $(r_{rx} + R_{eq})$ . Therefore, mathematically speaking, the three real unknowns  $M_1$ ,  $M_2$ , and  $R_{eq}$  are dependent, i.e., there are infinite combinations of  $(M_1, M_2, R_{eq})$  that can satisfy (6), and therefore, the actual value of  $M_1$ ,  $M_2$ , and  $R_{eq}$  cannot be solved. One simple example is as follows. Given the combination of  $(M_1, M_2, R_{eq})$  that satisfies (6), the combination of  $(aM_1, aM_2, (a^2 - 1)r_{rx} + a^2 R_{eq})$  also satisfies (6) for any nonzero constant  $a$ .

In fact, from (6), the ratio of  $M_1$  to  $M_2$  can be calculated. The same term  $(\omega_0^2 M_1 M_2 / (r_{rx} + R_{eq}) + j\omega_0 M_{12})$  appears in both rows of (6), and can be eliminated. The model becomes

$$M_1^2 / (r_{rx} + R_{eq}) - \tilde{I}_{tx2,1}^2 / \tilde{I}_{tx1,1}^2 \cdot M_2^2 / (r_{rx} + R_{eq}) = Z_{meas} \quad (7)$$

where  $Z_{meas} = [V_{C1,1} I_{tx1,1} - V_{C2,1} I_{tx2,1} - I_{tx1,1}^2 (j\omega_0 L_1 + r_{tx1}) + I_{tx2,1}^2 (j\omega_0 L_2 + r_{tx2})] / (\omega_0^2 I_{tx1,1}^2)$  is a complex number that can be calculated via available measurements and known system parameters. In (7), the two real terms  $t_1 = M_1^2 / (r_{rx} + R_{eq})$  and  $t_2 = M_2^2 / (r_{rx} + R_{eq})$  can be treated as two unknowns. With the real and imaginary parts of (7),  $t_1$  and  $t_2$  can be solved as follows:

$$\begin{aligned} t_1 &= \text{Re}(Z_{meas}) \\ &\quad - \text{Re}(\tilde{I}_{tx2,1}^2 / \tilde{I}_{tx1,1}^2) \cdot \text{Im}(Z_{meas}) / \text{Im}(I_{tx2,1}^2 / I_{tx1,1}^2) \\ t_2 &= -\text{Im}(Z_{meas}) / \text{Im}(\tilde{I}_{tx2,1}^2 / \tilde{I}_{tx1,1}^2) \end{aligned} \quad (8)$$

where  $\text{Re}(\cdot)$  and  $\text{Im}(\cdot)$  represent the real and imaginary parts of the variable  $(\cdot)$ . From the definitions of  $t_1$  and  $t_2$

$$M_1 / M_2 = \sqrt{t_1 / t_2}. \quad (9)$$

To sum up, for 2TX-1RX WPT systems, with the modeling method 1 (the equivalent resistor model), the actual value of  $M_1$ ,  $M_2$ , and  $R_{eq}$  cannot be solved if the system operates at the resonant frequency.

3) *Modeling Method 2: Equivalent Square Wave Source Model*: To overcome the limitation of the modeling method with an equivalent resistor, more information should be provided. For existing parameter identification methods with equivalent resistor load models, to obtain additional information, techniques such as: 1) communication from the receiver side [11], [26], [29]; 2) auxiliary circuits [16], [17]; 3) off-resonant frequency operation [19]; and 3) frequency

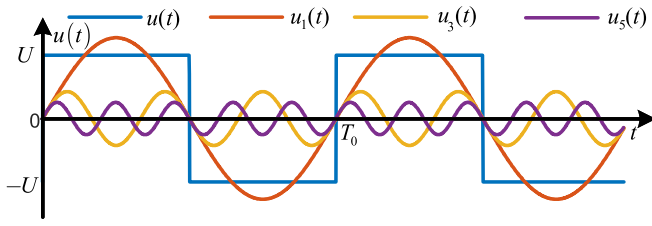


Fig. 4. Waveforms and harmonic components of square wave source  $u(t)$ .

sweeping [22] are applied to solve the dependency problem between  $M$  and  $R_{\text{eq}}$ . However, these techniques could result in increased hardware cost and system implementation complexity (categories  $a$ ,  $b$ , and  $d$ ), and suboptimal operation of the system (category  $c$ ).

In fact, high-order harmonics is an intuitive way to provide additional information, and it is widely applied to parameter identification problems [31], [32], [33], [34], [35]. However, model (4) with an equivalent resistor load cannot be directly extended to high-order harmonics, because the ac equivalent load  $R_{\text{eq}}$  is calculated based on the power analysis under fundamental frequency. To utilize the high-order harmonics information, the square wave source model in Fig. 3(b) can be adopted to model the 2TX–1RX LCC-S WPT system.

For the load part in Fig. 1, due to the capacitance  $C_0$ , the voltage at the terminal of  $R$  is close to a constant. Therefore, the voltage  $u$  at the terminals of the rectifier is very close to a square wave. For the  $n$ th harmonic, the following equation describes the KVL law on the RX coil:

$$\tilde{U}_n = jn\omega_s M_1 \tilde{I}_{\text{tx},n} + jn\omega_s M_2 \tilde{I}_{\text{tx},n} - \tilde{I}_{\text{rx},n} Z_{r,n} \quad (10)$$

where  $\tilde{U}_n$  is the  $n$ th harmonic of the square wave  $u(t)$ , and  $Z_{r,n}$  is the  $n$ th harmonic series impedance of the receiver side  $Z_{r,n} = jn\omega_s L_{\text{rx}} - j/(n\omega_s C_{\text{rx}}) + r_{\text{rx}}$ .

With the transmitter side model (1) and the equivalent square wave source model in (10), the overall system model is (11). Note that the model holds for any harmonic order  $n$

$$\begin{aligned} \tilde{V}_{C_1,n} &= \tilde{I}_{\text{tx},n} Z_{1,n} - jn\omega_s M_1 \tilde{I}_{\text{rx},n} + jn\omega_s M_{12} \tilde{I}_{\text{tx},n} \\ \tilde{V}_{C_2,n} &= \tilde{I}_{\text{tx},n} Z_{2,n} - jn\omega_s M_2 \tilde{I}_{\text{rx},n} + jn\omega_s M_{12} \tilde{I}_{\text{tx},n} \\ \tilde{U}_n &= jn\omega_s M_1 \tilde{I}_{\text{tx},n} + jn\omega_s M_2 \tilde{I}_{\text{tx},n} - \tilde{I}_{\text{rx},n} Z_{r,n}. \end{aligned} \quad (11)$$

In (11), for the  $n$ th harmonic, the model consists of three complex equations.  $\tilde{V}_{C_1,n}$ ,  $\tilde{I}_{\text{tx},n}$ ,  $\tilde{V}_{C_2,n}$ , and  $\tilde{I}_{\text{tx},n}$  and  $\omega_s$ ,  $Z_{1,n}$ ,  $Z_{2,n}$ , and  $Z_{r,n}$  are the known measurements and parameters, respectively. By separating (11) into real and imaginary parts, the model has six real equations and seven real unknown states:  $\tilde{U}_n$  and  $\tilde{I}_{\text{rx},n}$  are the two complex variables consisting of four real unknowns, and  $M_1$ ,  $M_2$ , and  $M_{12}$  are three unknown real variables. Compared with (4), the model (11) does not have the real unknown  $R_{\text{eq}}$ , but with two additional real unknown variables (real and imaginary parts of  $\tilde{U}_n$ ).

With the analysis of the square wave source  $u(t)$ , the relationship among variables of different harmonics can also be derived. For example, with the typical WPT inverter duty cycle of 0.5, the square wave source  $u(t)$  is shown as the blue curve in Fig. 4 (with the magnitude of  $U$ ). According to the Fourier series,  $u(t) = a_0 + \sum_{n=1}^{\infty} (a_n \cos(n\omega t) + b_n \sin(n\omega t))$ ,

the coefficients can be calculated as  $a_0 = a_n = 0$  and  $b_n = (2/T) \int_0^T u(t) \sin(n\omega t) dt = \frac{4U}{\pi n}$ ,  $n = 1, 3, 5, \dots$ . Therefore,  $u(t)$  can be rewritten into the sum of harmonic components  $u_n(t)$  as (12). These components are also shown in Fig. 4

$$u(t) = \sum_{n=1}^{\infty} u_n(t) = \sum_{n=1}^{\infty} 4U \sin(n\omega t) / (\pi n), \quad n = 1, 3, 5, \dots \quad (12)$$

From (12), the relationship between the  $n$ th harmonic component magnitude  $U_n$  and the fundamental component magnitude  $U_1$  is shown in the following equation:

$$U_n / U_1 = 1/n. \quad (13)$$

Therefore, if different harmonic components (the fundamental frequency and high harmonic components) are considered, the model will have  $6p$  real equations from (11) and  $p - 1$  equations from (13), where  $p$  is a positive integer and is the number of discrete harmonic order. The unknown states are  $M_1$ ,  $M_2$ , and  $M_{12}$  (three real unknowns) and  $\tilde{U}_n$  and  $\tilde{I}_{\text{rx},n}$  ( $4p$  real unknowns). To ensure that the redundancy is adequate, the number of equations should not be smaller than that of unknown states, i.e.,  $6p + p - 1 \geq 3 + 4p$ , or  $p \geq 2$ . For example, the fundamental frequency and the third harmonic components can be selected as the components of interest to solve the unknowns.

4) *Parameter Independency at Resonant Frequency Using Modeling Method 2*: In fact, the condition  $p \geq 2$  is necessary but may not be sufficient. This means that the unknowns may still not be solved if the parameters are dependent. One obvious example is the modeling method 1 at the resonant frequency: although with six equations and six unknowns, the parameters  $M_1$  and  $M_2$  still cannot be solved. Therefore, the parameter independency using the modeling method 2 should be carefully evaluated.

For the  $n$ th harmonic model in (11), eliminate the transmitter side current  $\tilde{I}_{\text{rx},n}$  in the first two rows using the third row

$$\begin{aligned} \tilde{V}_{C_1,n} &= \tilde{I}_{\text{tx},n} Z_{1,n} + (jn\omega_s M_1 \tilde{U}_n + n^2 \omega_s^2 M_1^2 \tilde{I}_{\text{tx},n}) / Z_{r,n} \\ &\quad + (n^2 \omega_s^2 M_1 M_2 / Z_{r,n} + jn\omega_s M_{12}) \tilde{I}_{\text{tx},n} \\ \tilde{V}_{C_2,n} &= \tilde{I}_{\text{tx},n} Z_{2,n} + (jn\omega_s M_2 \tilde{U}_n + n^2 \omega_s^2 M_2^2 \tilde{I}_{\text{tx},n}) / Z_{r,n} \\ &\quad + (n^2 \omega_s^2 M_2 M_1 / Z_{r,n} + jn\omega_s M_{12}) \tilde{I}_{\text{tx},n}. \end{aligned} \quad (14)$$

Next, in (14), eliminate the complex variable  $\tilde{U}_n$  with the second row

$$\begin{aligned} \tilde{V}_{C_1,n} &= \tilde{I}_{\text{tx},n} Z_{n1} + \tilde{V}_{C_2,n} \frac{M_1}{M_2} - \frac{M_1}{M_2} \tilde{I}_{\text{tx},n} Z_{n2} \\ &\quad + jn\omega_s M_{12} \left( \tilde{I}_{\text{tx},n} - \frac{M_1}{M_2} \tilde{I}_{\text{tx},n} \right). \end{aligned} \quad (15)$$

From (15), the  $n$ th harmonic model after simplification is a function of two real variables  $M_1/M_2$  and  $M_{12}$ . With the real and imaginary parts of the model,  $M_{12}$  and  $M_1/M_2$  can be solved. However, one can observe that the mutual inductances  $M_1$  and  $M_2$  are always coupled and are dependent. This dependency still exists even when  $p \geq 2$ .

Fortunately, (13) introduces additional information to decouple  $M_1$  and  $M_2$ . For example, when the fundamental

frequency and the third harmonic components are utilized ( $p = 2$ ), the relationship  $U_3/U_1 = 1/3$  is the key to ensuring both  $M_1$  and  $M_2$  are solvable. One can observe that, if one substitutes the first row into the third row of (11), the variable  $\tilde{I}_{rx,n}$  can be eliminated, and  $\tilde{U}_n$  is a function of  $M_1$ ,  $M_2$ , and  $M_{12}$  as follows:

$$\begin{aligned} \tilde{U}_n = & jn\omega_s M_1 \tilde{I}_{tx1,n} + jn\omega_s M_2 \tilde{I}_{tx2,n} \\ & + (j\tilde{I}_{tx1,n} Z_{1,n} Z_{r,n} - j\tilde{V}_{C1,n} Z_{r,n} \\ & - n\omega_s M_{12} \tilde{I}_{tx2,n} Z_{r,n}) / (n\omega_s M_1). \end{aligned} \quad (16)$$

Therefore, for  $n = 1$  or  $3$ , substitute the magnitude of the above expression  $\tilde{U}_n$  into  $U_3/U_1 = 1/3$ , and an additional equation independent of (15) is obtained which is related to  $M_1$ ,  $M_2$ , and  $M_{12}$ . Consequently,  $M_1$ ,  $M_2$ , and  $M_{12}$  can be solved and the solution is unique. On the contrary, if the modeling method 1 is utilized, the equivalent resistor only holds for the fundamental frequency component; in this case, the modeling method 1 cannot adopt information of higher order harmonics, and the parameters  $M_1$  and  $M_2$  are still dependent and cannot be solved.

The previous theoretical analysis shows the reason why the parameters are independent and can be solved using modeling method 2. Besides, the dependency of parameters can also be numerically validated through the rank of the Jacobian matrix of the system model. For an overdetermined equation, if the rank of the Jacobian matrix is equal to the number of unknown states, the system parameters are independent; if the rank of the Jacobian matrix is smaller than the number of unknown states, the system parameters are dependent. For this case, if the  $n$ th harmonic model in (11) is considered for both  $n = 1$  and  $3$  and (13) is not considered, the rank of the Jacobian matrix (with the dimension of  $12 \times 11$ ) is 10. If (13) is also considered in addition to the  $n$ th harmonic model in (12) ( $n = 1$  and  $3$ ), the rank of the Jacobian matrix (with the dimension of  $13 \times 11$ ) is 11, which is equal to the number of unknowns. Therefore, numerical results are consistent with the above theoretical derivation.

5) *Consideration of Mutual Inductance  $M_{12}$* : Throughout the previous modeling procedure, the mutual inductance between the two TX coils ( $M_{12}$ ) is treated as an unknown state to be estimated. In practical two-transmitter WPT systems, the two TX coils are usually placed such that  $M_{12}$  is 0, to decouple the two coils [40]. Therefore, it is also plausible to assume  $M_{12} = 0$  and eliminate the unknown variable  $M_{12}$ .

In fact, the advantages of the modeling method 2 compared with the modeling method 1 still hold even when  $M_{12}$  is known to be 0. For the modeling method 1, even if  $M_{12} = 0$  in (6), there are still infinite combinations of  $M_1$ ,  $M_2$ , and  $R_{eq}$  that can satisfy (6), i.e., the parameters to be solved are still dependent. For the modeling method 2, even if  $M_{12} = 0$  in (15), the parameters  $M_1$  and  $M_2$  are still dependent, and it is necessary to include (13) into the model; the parameters become independent if  $p = 2$  and (13) is included into the model. Therefore, the conclusions are similar no matter whether  $M_{12}$  is treated as a constant (zero) or an unknown state.

### III. SOLUTION VIA STATE ESTIMATION

From Section II, the modeling method 2 (equivalent square wave source model) is adopted. Compared with the modeling method 1 (equivalent resistor model), the modeling method 2 ensures that the parameters are independent and can be estimated. For the 2TX-1RX WPT system, the first- and third-harmonic components are utilized to build the overall model, with 13 real equations and 11 real unknown states. To simplify the expression, the equation  $U_3 = U_1/3$  is substituted into the rest of the equations to eliminate the unknown variable  $U_3$ , resulting in 12 real equations and ten real unknown states. The overall model is shown in (17).  $(\cdot)_{n,r}$  and  $(\cdot)_{n,i}$  represents the real and imaginary parts of the  $n$ th harmonic component of the corresponding variable  $(\cdot)$ , respectively.  $\tilde{U}_n = U_n \angle \theta_n$ ,  $U_{n,r} = U_n \cos \theta_n$ ,  $U_{n,i} = U_n \sin \theta_n$ , and  $\tilde{I}_{rx,n} = I_{rx,n} \angle \varphi_n$

$$\begin{aligned} 0 = & \left( \frac{1}{\omega_s C_{tx1}} - \omega_s L_{tx1} \right) I_{tx1,1,i} + r_{tx1} I_{tx1,1,r} + \omega_s M_1 I_{rx,1,i} \\ & - \omega_s M_{12} I_{tx2,1,i} - V_{C1,1,r} \\ 0 = & \left( \omega_s L_{tx1} - \frac{1}{\omega_s C_{tx1}} \right) I_{tx1,1,r} + r_{tx1} I_{tx1,1,i} - \omega_s M_1 I_{rx,1,r} \\ & + \omega_s M_{12} I_{tx2,1,r} - V_{C1,1,i} \\ 0 = & \left( \frac{1}{\omega_s C_{tx2}} - \omega_s L_{tx2} \right) I_{tx2,1,i} + r_{tx2} I_{tx2,1,r} + \omega_s M_2 I_{rx,1,i} \\ & - \omega_s M_{12} I_{tx1,1,i} - V_{C2,1,r} \\ 0 = & \left( \omega_s L_{tx2} - \frac{1}{\omega_s C_{tx2}} \right) I_{tx2,1,r} + r_{tx2} I_{tx2,1,i} - \omega_s M_2 I_{rx,1,r} \\ & + \omega_s M_{12} I_{tx1,1,r} - V_{C2,1,i} \\ 0 = & \left( \omega_s L_{rx} - \frac{1}{\omega_s C_{rx}} \right) I_{rx,1,i} - r_{rx} I_{rx,1,r} - \omega_s M_1 I_{tx1,1,i} \\ & - \omega_s M_2 I_{tx2,1,i} - U_1 \cos \theta_1 \\ 0 = & \left( \frac{1}{\omega_s C_{rx}} - \omega_s L_{rx} \right) I_{rx,1,r} - r_{rx} I_{rx,1,i} + \omega_s M_1 I_{tx1,1,r} \\ & + \omega_s M_2 I_{tx2,1,r} - U_1 \sin \theta_1 \\ 0 = & \left( \frac{1}{3\omega_s C_{tx1}} - 3\omega_s L_{tx1} \right) I_{tx1,3,i} + r_{tx1} I_{tx1,3,r} + 3\omega_s M_1 I_{rx,3,i} \\ & - 3\omega_s M_{12} I_{tx2,3,i} - V_{C1,3,r} \\ 0 = & \left( 3\omega_s L_{tx1} - \frac{1}{3\omega_s C_{tx1}} \right) I_{tx1,3,r} + r_{tx1} I_{tx1,3,i} - 3\omega_s M_1 I_{rx,3,r} \\ & + 3\omega_s M_{12} I_{tx2,3,r} - V_{C1,3,i} \\ 0 = & \left( \frac{1}{3\omega_s C_{tx2}} - 3\omega_s L_{tx2} \right) I_{tx2,3,i} + r_{tx2} I_{tx2,3,r} + 3\omega_s M_2 I_{rx,3,i} \\ & - 3\omega_s M_{12} I_{tx1,3,i} - V_{C2,3,r} \\ 0 = & \left( 3\omega_s L_{tx2} - \frac{1}{3\omega_s C_{tx2}} \right) I_{tx2,3,r} + r_{tx2} I_{tx2,3,i} - 3\omega_s M_2 I_{rx,3,r} \\ & + 3\omega_s M_{12} I_{tx1,3,r} - V_{C2,3,i} \\ 0 = & \left( 3\omega_s L_{rx} - \frac{1}{3\omega_s C_{rx}} \right) I_{rx,3,i} - r_{rx} I_{rx,3,r} \\ & - 3\omega_s (M_1 I_{tx1,3,i} + M_2 I_{tx2,3,i}) - \frac{U_1 \cos \theta_3}{3} \\ 0 = & \left( \frac{1}{3\omega_s C_{rx}} - 3\omega_s L_{rx} \right) I_{rx,3,r} - r_{rx} I_{rx,3,i} \\ & + 3\omega_s (M_1 I_{tx1,3,r} + M_2 I_{tx2,3,r}) - \frac{U_1 \sin \theta_3}{3}. \end{aligned} \quad (17)$$

The overall model for parameter identification can be rewritten in a standard format

$$\mathbf{0} = \mathbf{h}(\mathbf{x}) \quad (18)$$

where  $\mathbf{h}(\mathbf{x}) = [h_1(x), h_2(x), \dots, h_{12}(x)]^T$  corresponding to the right side of (17). The known coefficients in  $\mathbf{h}(\mathbf{x})$  include available measurements  $V_{C1,1,r}, V_{C1,1,i}, V_{C2,1,r}, V_{C2,1,i}, V_{C1,3,r}, V_{C1,3,i}, V_{C2,3,r}, V_{C2,3,i}, I_{tx1,1,r}, I_{tx1,1,i}, I_{tx2,1,r}, I_{tx2,1,i}, I_{tx1,3,r}, I_{tx1,3,i}, I_{tx2,3,r},$  and  $I_{tx2,3,i}$ , and available parameters  $\omega_s, L_{tx1}, C_{tx1}, L_{tx2}, C_{tx2}, L_{rx}, C_{rx}, r_{tx1}, r_{tx2},$  and  $r_{rx}$ . The state vector to be estimated is  $\mathbf{x} = [M_1, M_2, M_{12}, U_1, \theta_1, \theta_3, I_{rx,1,r}, I_{rx,1,i}, I_{rx,3,r},$  and  $I_{rx,3,i}]^T \in \mathbb{R}^{10 \times 1}$ . Note that if  $M_{12}$  is known, the variable  $M_{12}$  can be removed from the state vector, and  $\mathbf{x} = [M_1, M_2, U_1, \theta_1, \theta_3, I_{rx,1,r}, I_{rx,1,i}, I_{rx,3,r}, I_{rx,3,i}]^T \in \mathbb{R}^{9 \times 1}$ .  $\mathbf{h}(\mathbf{x})$  is a nonlinear function of the state vector.

To solve the state vector  $\mathbf{x}$  in the nonlinear model (18), there are extensive ways including EKF, machine learning, adaptive evolution, and Newton's method [13], [21], [22], [31], [32], [33], [34], [35]. Here, Newton's method is applied to solve (18). The estimation problem first can be converted into an optimization problem as follows:

$$\min_{\mathbf{x}} J = \mathbf{h}(\mathbf{x})^T \mathbf{W} \mathbf{h}(\mathbf{x}) \quad (19)$$

where the weight matrix is  $\mathbf{W} = \text{diag}([\dots \ 1/\sigma_i \ \dots])$ , and  $\sigma_i$  is the standard deviation of the  $i$ th measurement. The best estimated state vector  $\hat{\mathbf{x}}$  can be calculated with the iteration in (20) until convergence [41]

$$\mathbf{x}^{v+1} = \mathbf{x}^v - (\mathbf{H}^T \mathbf{W} \mathbf{H})^{-1} \mathbf{H}^T \mathbf{W} (\mathbf{h}(\mathbf{x}^v) - \mathbf{z}) \quad (20)$$

where  $\mathbf{H} = \partial \mathbf{h} / \partial \mathbf{x}|_{\mathbf{x}=\mathbf{x}^v}$  is the Jacobian matrix. The element  $H_{ij}$  at the  $i$ th row and the  $j$ th column of  $\mathbf{H}$  represents the partial derivative of the  $i$ th function  $h_i(x)$  to the  $j$ th state  $x_j$  in the state vector  $\mathbf{x}$ , i.e.,  $H_{ij} = \partial h_i / \partial x_j|_{\mathbf{x}=\mathbf{x}^v}$ .

#### IV. APPLICATIONS OF ESTIMATED STATES

With the estimated states, the following parameters and operating conditions can be obtained, including the mutual inductances ( $M_1, M_2$ ), the load voltages ( $\tilde{U}_1, \tilde{U}_3$ ), and the load currents ( $\tilde{I}_{rx,1}, \tilde{I}_{rx,3}$ ). Based on those estimated variables, further control can be conducted for better performance of the system. Here, three typical controls are introduced as examples, including maximum efficiency control, constant voltage control, and constant current control, to show the advantages of mutual inductances and load tracking.

##### A. Maximum Efficiency Control

From [25], for the 2TX-1RX WPT system, if the two TX coils are close to identical, and the currents through the TX coils meet  $\tilde{I}_{tx1}/\tilde{I}_{tx2} = k_1/k_2$ , the energy transfer efficiency will reach the maximum. Here,  $k_1$  and  $k_2$  represent the coupling coefficient corresponding to the mutual inductances  $M_1$  and  $M_2$ . With the characteristics of the LCC topology and the estimated mutual inductances  $M_1$  and  $M_2$ , the input voltage can be regulated as follows [25]:

$$\frac{\tilde{I}_{tx1}}{\tilde{I}_{tx2}} = \frac{C_1 \tilde{V}_{in1}}{C_2 \tilde{V}_{in2}} = \frac{k_1}{k_2} \Rightarrow \frac{\tilde{V}_{in1}}{\tilde{V}_{in2}} = \frac{C_2 k_1}{C_1 k_2} \Rightarrow \frac{V_{d1}}{V_{d2}} = \frac{C_2 k_1}{C_1 k_2}. \quad (21)$$

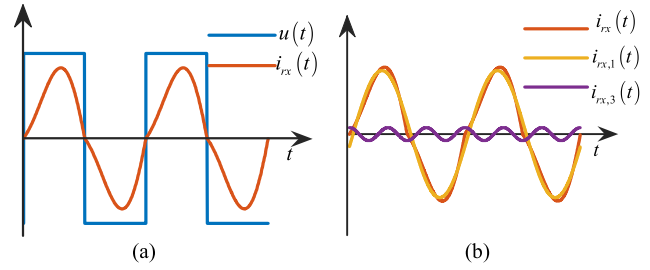


Fig. 5. (a) Input voltage and current of the rectifier. (b) First- and third-harmonic components of the input current of the rectifier.

##### B. Constant Voltage Control

With the estimated voltage phasor  $\tilde{U}_1$  at the input of the rectifier, the dc output voltage  $V_{out}$  at terminals of  $R$  can be approximated as follows:

$$V_{out} = \pi U_1 / 4 - 2V_F \quad (22)$$

where  $V_F$  is the forward voltage of the diodes in the rectifier. In fact, the voltage  $U_1$  should be proportional to the dc input power supply voltages [25], namely,  $V_{d1}$  at transmitter 1 and  $V_{d2}$  at transmitter 2. To achieve the constant voltage control and keep the dc output voltage as  $V_{out,set}$ , the dc input voltages can be adjusted as  $V_{d1,set}$  and  $V_{d2,set}$ . With the present dc input voltages  $V_{d1}, V_{d2}$ , present dc output voltage  $V_{out}$ , and the target dc output voltage  $V_{out,set}$ , the values of  $V_{d1,set}$  and  $V_{d2,set}$  can be calculated as follows:

$$\frac{V_{d1}}{V_{d1,set}} = \frac{V_{d2}}{V_{d2,set}} = \frac{V_{out} + 2V_F}{V_{out,set} + 2V_F}. \quad (23)$$

##### C. Constant Current Control

The estimated current phasors  $\tilde{I}_{rx,1}$  and  $\tilde{I}_{rx,3}$  at the input of the rectifier can be rewritten as  $I_{rx1} \angle \varphi_1$  and  $I_{rx3} \angle \varphi_3$ , respectively. The estimated voltage phasor  $\tilde{U}_1 = U_1 \angle \theta_1$ . Here, we assume  $i_{rx}(t) = i_{rx,1}(t) + i_{rx,3}(t)$ , since the contributions of other harmonic components are small and are neglected for simplicity. Due to the characteristics of the rectifier, the zero crossing time instant (negative to positive) of  $u(t)$  and  $i_{rx}(t)$  at which  $u(t)$  and  $i_{rx}(t)$  cross zero is equal, as shown in Fig. 5(a). If the phase  $(\theta_1 + 90^\circ)$  is selected as the new reference, the corresponding phasors become  $\tilde{U}_1 = U_1 \angle -90^\circ$ ,  $\tilde{I}_{rx1} = I_{rx1} \angle (\varphi_1 - \theta_1 - 90^\circ)$ , and  $\tilde{I}_{rx3} = I_{rx3} \angle (\varphi_3 - \theta_1 - 90^\circ)$ . In this case, the zero crossing time instant (negative to positive) is equal to 0 for both  $u(t)$  and  $i_{rx}(t)$ . With this new reference, the time-domain waveforms  $i_{rx}(t)$ ,  $i_{rx,1}(t)$ , and  $i_{rx,3}(t)$  are shown in Fig. 5(b).

Due to the characteristics of the rectifier and the steady state operation of the system, the dc output current  $I_{out}$  through the load  $R$  can be approximated as the average value of  $|i_{rx}(t)|$  as shown in the following equation:

$$\begin{aligned} I_{out} &= \frac{1}{2\pi/\omega_s} \int_0^{2\pi/\omega_s} |i_{rx}(t)| dt = \frac{1}{\pi/\omega_s} \int_0^{\pi/\omega_s} i_{rx}(t) dt \\ &= \frac{1}{\pi} \int_0^\pi [I_{rx,1} \sin(\omega_s t + \varphi_1 - \theta_1) \\ &\quad + I_{rx,3} \sin(3\omega_s t + \varphi_3 - \theta_1)] d(\omega_s t) \\ &= \frac{2}{\pi} \left( I_{rx1} \cos(\varphi_1 - \theta_1) + \frac{I_{rx3}}{3} \cos(\varphi_3 - \theta_1) \right). \quad (24) \end{aligned}$$

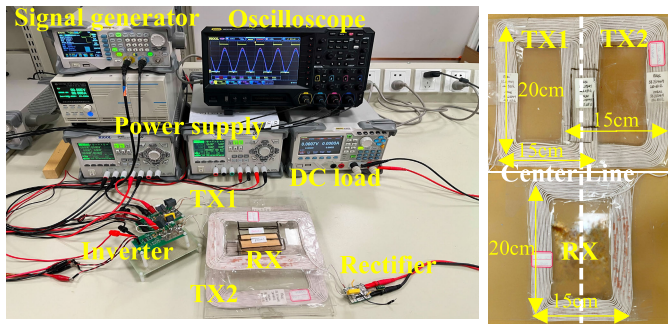


Fig. 6. Experimental setup.

In fact, with (22) and (24), the value of the load can be directly calculated as  $R = V_{out}/I_{out}$ ; in this case, the target output voltage to keep constant current can be calculated, and the output voltage can be controlled according to (23). An alternative way is to directly design the control strategy similar as (23): if one assumes that  $V_F$  is relatively small and can be neglected, the dc output current  $I_{out}$  is proportional to  $V_{d1}$  and  $V_{d2}$ . To keep the dc output current as  $I_{out,set}$ , the dc input voltages can be adjusted as  $V_{d1,set}$  and  $V_{d2,set}$ . With the present dc input voltages  $V_{d1}$  and  $V_{d2}$ , present dc output current  $I_{out}$ , and the target dc output current  $I_{out,set}$ , the values of  $V_{d1,set}$  and  $V_{d2,set}$  can be calculated as (25). Note that the alternative way is simpler but with slightly larger error after neglecting  $V_F$ . In this article, the alternative way is selected as an example for the constant current control

$$\frac{V_{d1}}{V_{d1,set}} = \frac{V_{d2}}{V_{d2,set}} = \frac{I_{out}}{I_{out,set}}. \quad (25)$$

## V. HARDWARE EXPERIMENTS

This section verifies the effectiveness of the proposed mutual inductances and load tracking method via hardware experiments.

### A. Experimental Setup

Fig. 6 shows a prototype of the 2TX–1RX LCC-S WPT system. The topology is as same as that shown in Fig. 1. According to different practical applications, the output power and dimension of the system can be scaled up or down.

The two power supplies provide dc input to the circuit with the initial value as  $V_{d1} = V_{d2} = 40$  V. The two half-bridge inverters are controlled with the same strategy. The switching signals of both inverters are generated with a duty cycle of 0.5. The two TX coils (TX1 and TX2) and one RX coil are wound using the Litz wire with the same dimension ( $15 \times 20$  cm). The relative locations of TX coils are fixed: there is an overlap area between TX1 and TX2 as shown in the figure to decouple the two TX coils ( $M_{12} = 0$ ). This strategy is widely adopted in practical WPT systems to avoid coupling between TX coils. The location of RX can vary, resulting in different values of  $M_1$  and  $M_2$ . The rectifier consists of four diodes (DFLS240L-7), with the forward voltage  $V_F = 0.4$  V. An electronic dc load provides a varying load  $R$  for the system. The other parameters of the system are shown in Table I, with actual values measured by the LCR meter. The operating

TABLE I  
WPT SYSTEM PARAMETERS

Transmitter #1 (TX1)	Transmitter #2 (TX2)	Receiver (RX)
$L_1 = 29.27 \mu\text{H}$	$L_2 = 25.53 \mu\text{H}$	
$C_1 = 91.94 \text{ nF}$	$C_2 = 110 \text{ nF}$	
$L_{rx1} = 57.43 \mu\text{H}$	$L_{rx2} = 58.76 \mu\text{H}$	$L_{rx} = 59.14 \mu\text{H}$
$C_{rx1} = 83 \text{ nF}$	$C_{rx2} = 71 \text{ nF}$	$C_{rx} = 42 \text{ nF}$
$r_{rx1} = 0.148 \Omega$	$r_{rx2} = 0.150 \Omega$	$r_{rx} = 0.154 \Omega$

frequency is the same as the resonant frequency of the system, i.e., 100 kHz.

The harmonics (including the fundamental frequency component) of measurements  $v_{in1}$ ,  $v_{C1}$ ,  $v_{in2}$ , and  $v_{C2}$  need to be extracted for parameter identification. There are many methods to estimate the harmonics of signals. Discrete Fourier transform (DFT) and fast Fourier Transform (FFT) are widely applied to electric machinery and power electronics to analyze the steady state signals [31], [32]. For power systems, recursive least square (RLS), Kalman filter (KF), and enhanced phase-locked loop (EPLL)-based method are recursive techniques usually adopted to estimate the time-varying signal in real time to track the dynamics [36], [37], [38], [39]. In this article, the standard FFT method is applied to extract harmonics, since the operation of WPT systems can be seen as steady state. Data acquisitions via the oscilloscope are one of the ways in the literature to simplify the experiments [15], [19], [21], [22], [23], [30]. Oscilloscopes are applied since its high accuracy, sufficient bandwidth, and simple for such validating experiments. Here, the waveforms of voltage measurements  $v_{in1}$ ,  $v_{in2}$ ,  $v_{C1}$ , and  $v_{C2}$  are sampled and recorded by the oscilloscope (RIGOL MSO5104). Note that the proposed method does not require any current measurements, and therefore, the data acquisition procedure is much simplified. The sampling rate is 5 MHz. The harmonics are extracted using the waveforms of 5 cycles of the resonant frequency, i.e., 50  $\mu\text{s}$ . The measured waveforms are then fed into the computer and analyzed by MATLAB.

### B. State Estimation Results

*Case 1 (Example Operating Condition):* This case verifies the proposed mutual inductances and load tracking method at an example operation condition. RX is placed close to the center of the two TX coils (TX1 and TX2). The vertical distance between TX and RX is 2.3 cm. The actual values of the mutual inductances  $M_1$  and  $M_2$  and the load  $R$  are  $M_1 = 14.6 \mu\text{H}$ ,  $M_2 = 14.1 \mu\text{H}$ , and  $R = 30 \Omega$ . The actual output dc voltage  $V_{out}$  and current  $I_{out}$  are 21.74 V and 0.7263 A, respectively. Next, the states are estimated using the available measurements only at the transmitter side (four voltage measurements), as shown in Fig. 7(a).

With the proposed modeling framework in (17) and the proposed parameter identification method in (20), the results of the estimated  $M_1$  and  $M_2$  are depicted in Fig. 8.

In Fig. 8, the dotted line represents the actual values of  $M_1$  and  $M_2$ . It can be seen the method quickly converges to the actual value after only several iterations. The estimated mutual inductances are  $M_1 = 14.55 \mu\text{H}$  and  $M_2 = 14.04 \mu\text{H}$ ,

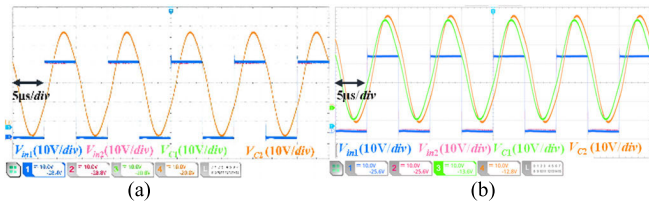


Fig. 7. Waveforms of measurements. (a) Case 1, first group,  $R = 30 \Omega$ . (b) Case 3, second group,  $R = 30 \Omega$ .

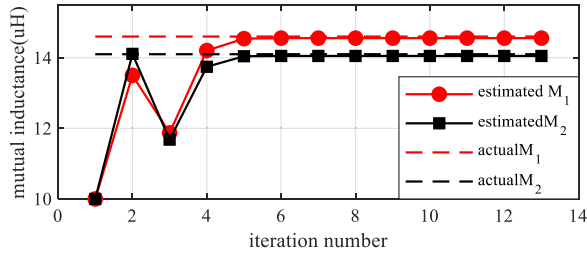


Fig. 8. Estimation results of mutual inductances, example operating condition.

with the estimation error of 0.34% and 0.43%, respectively. Similarly, other state variables also converge with acceptable accuracy. The fundamental frequency component of the output square voltage is estimated as  $\tilde{U}_1 = 28.169\angle -91.10^\circ \text{V}$ . The RX coil currents are  $\tilde{I}_{\text{rx},1} = 1.157\angle -93.48^\circ \text{A}$  and  $\tilde{I}_{\text{rx},3} = 0.1186\angle 4.112^\circ \text{A}$ . Therefore, the output dc voltage can be calculated as 21.32 V according to (22), and the output dc current can be calculated as 0.7336 A according to (24). The estimation errors are 1.93% for the output dc voltage and 1.01% for the output dc current.

The way to select initial states values for the iteration procedure is presented below. Since  $M_{12} = 0$ , there are nine states, i.e.,  $\mathbf{x} = [M_1, M_2, U_1, \theta_1, \theta_3, I_{\text{rx},1,r}, I_{\text{rx},1,i}, I_{\text{rx},3,r}, I_{\text{rx},3,i}]$ . The initial values are randomly provided with certain boundaries considering typical operating points of the system, as follows.  $U_1 \in [10 \text{ V}, 50 \text{ V}]$ ,  $\theta_1, \theta_3 \in [-\pi/2, \pi/2]$ ,  $I_{\text{rx},1,r}$  and  $I_{\text{rx},1,i} \in [-2 \text{ A}, 2 \text{ A}]$ , and  $I_{\text{rx},3,r}$  and  $I_{\text{rx},3,i} \in [-0.2 \text{ A}, 0.2 \text{ A}]$ .  $M_1, M_2 \in [6, 30 \mu\text{H}]$  are selected according to the coupling coefficient  $k$  ranging from 0.1 to 0.5. Extensive results prove that the convergence region for this problem is quite large. For example, for combinations of initial values such as the lower boundary  $x_0 = [6 \mu\text{H}, 6 \mu\text{H}, 10 \text{ V}, -\pi/2, -\pi/2, -2 \text{ A}, -2 \text{ A}, -0.2 \text{ A}, -0.2 \text{ A}]$  and the upper boundary  $x_0 = [30 \mu\text{H}, 30 \mu\text{H}, 50 \text{ V}, \pi/2, \pi/2, 2 \text{ A}, 2 \text{ A}, 0.2 \text{ A}, 0.2 \text{ A}]$ , the algorithm took 14 and 14 steps to converge, respectively. In Fig. 8, the initial values are selected as  $x_0 = [10 \mu\text{H}, 10 \mu\text{H}, 25 \text{ V}, \pi/2, \pi/2, 1 \text{ A}, 1 \text{ A}, 0.1 \text{ A}, 0.1 \text{ A}]$ , and it took 13 steps to converge.

The computational burden of the parameter identification method is also analyzed. From (20), in each iteration step, the inverse of the matrix  $\mathbf{H}^T \mathbf{W} \mathbf{H}$  (with dimension of  $9 \times 9$ ) and multiplications of several matrices (with dimensions  $9 \times 9$ ,  $9 \times 12$ ,  $12 \times 12$ , and  $12 \times 1$ ) need to be calculated. Throughout this article, to simplify the experimental settings, the proposed method is implemented using MATLAB on a personal computer with Intel i7-7700 CPU. It takes less than 0.5 ms for one iteration step, and the 13 iteration steps are completed within 7 ms. For this example, operating condition

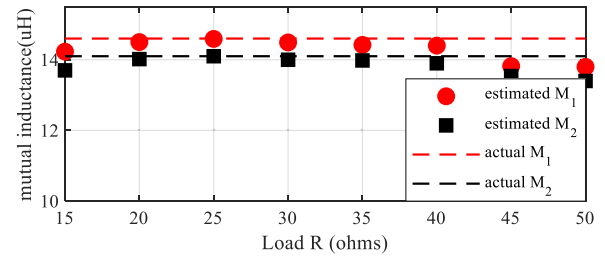


Fig. 9. Estimation results of mutual inductances, various loads.

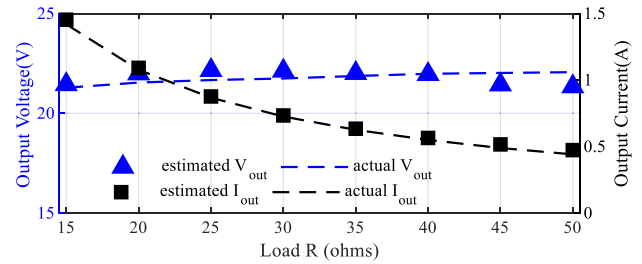


Fig. 10. Estimation results of output dc voltages and currents, various loads.

(case 1), the proposed method has also been implemented in a commonly used microcontroller TMS320F28335 based on a 32-bit MCU with an operating frequency of 150 MHz (6.67 ns per cycle). It takes 268 139 cycle for one iteration step ( $268\ 139 \times 6.67 \text{ ns} = 1.79 \text{ ms}$ ), and the 13 iteration steps takes 3 467 512 cycle ( $3\ 467\ 512 \times 6.67 \text{ ns} = 23.1 \text{ ms}$ ). The FFT analysis takes 38 803 cycle ( $38\ 803 \times 6.67 \text{ ns} = 0.259 \text{ ms}$ ). One can observe that the computational burden of the proposed method is not quite high, since the dimensions of matrices for inverse and multiplication are relatively small. It should also be noted that, for different applications and different types of microcontrollers, whether the computational burden can meet the practical requirement should be further evaluated.

*Case 2 (Variation of Loads):* This case demonstrates the state estimation results with various loads. The value of the load  $R$  varies from 15 to 50  $\Omega$ , with the step size of 5  $\Omega$ . Other system parameters keep the same as those in Case 1. The actual mutual inductances are still  $M_1 = 14.6 \mu\text{H}$  and  $M_2 = 14.1 \mu\text{H}$ . For each load, similar to case 1, the corresponding mutual inductances  $M_1$  and  $M_2$  and the voltage and current phasors of the receiver  $\tilde{U}_1$ ,  $\tilde{I}_{\text{rx},1}$ , and  $\tilde{I}_{\text{rx},3}$  can be estimated through several iterations. Afterward, the output dc voltage  $V_{\text{out}}$  and current  $I_{\text{out}}$  are calculated according to (22) and (24), respectively.

The estimated results of  $M_1$  and  $M_2$  with various loads are depicted in Fig. 9. One can observe that most estimated inductances are very close to the actual values, and the errors tend to increase when the value of  $R$  is too large or too small. The average absolute errors of  $M_1$  and  $M_2$  are 2% and 1.9%, respectively.

Fig. 10 depicts the estimated output dc voltages and currents  $V_{\text{out}}$  and  $I_{\text{out}}$  with various loads. In fact, load-independent dc voltage output is one of the merits of LCC topology, as one can observe that the blue dotted line is close to horizontal when the input voltages are constants and the load varies. As a result, the output current  $I_{\text{out}}$  will decrease while  $R$  increases.

From Fig. 10, the estimated output dc voltages and currents are consistent with the actual values. The average absolute estimation errors are around 2% for  $V_{out}$  and 3% for  $I_{out}$ . Note that even with load-independent characteristics of the output voltage, the constant voltage control in Section IV-B is still valuable: the output voltage can be regulated to a user-defined value  $V_{out,set}$ . Detailed experimental verification can be found in Section V-C.

*Case 3 (Variation of Mutual Inductances):* To further verify the effectiveness of the proposed method, the experiments with three groups of mutual inductances are conducted, with three different positions of RX. The first group of mutual inductances (position 1) is the same as that in cases 1 and 2, i.e.,  $M_1 = 14.6 \mu\text{H}$  and  $M_2 = 14.1 \mu\text{H}$ . The second group is achieved by moving RX horizontally to the right, 2 cm away from the center line (position 2). As a result, the coupling between TX1 and RX decreases, while the coupling between TX2 and RX increases:  $M_1 = 9.5 \mu\text{H}$  and  $M_2 = 19.4 \mu\text{H}$ . The third group is achieved by moving RX horizontally to the left, 1.7 cm away from the center line; at the same time, the vertical distance increases from 2.3 to 3 cm (position 3). As a result,  $M_1 = 16.1 \mu\text{H}$  and  $M_2 = 9.0 \mu\text{H}$ . For each position of RX, the load varies from 15 to 50  $\Omega$ , with a step size of 5  $\Omega$ . Fig. 7(b) shows the measurement waveforms of an example case in the second group (position 2), and in this case, the load is 30  $\Omega$ . It can be seen that the voltage across the capacitances  $v_{C1}(t)$  and  $v_{C2}(t)$  also deviates from the example case in the first group, as shown in Fig. 7(a). The reason lies in the mutual inductance variation. Fig. 11(a)–(c) shows the parameter identification results of mutual inductances  $M_1$  and  $M_2$ ,  $V_{out}$ , and  $I_{out}$ , respectively, with different positions of RX and different loads. One can observe that the estimation results of mutual inductances are quite accurate and are close to the actual values. The average estimation errors of  $M_1$  and  $M_2$  are 1.91% and 1.75%, respectively. The values of  $V_{out}$  and  $I_{out}$  can also be accurately estimated, with average errors of 3% and 2.8%, respectively. The results indicate the estimation method can work accurately with various mutual inductances.

### C. Control Applications

This section verifies the control applications enabled by the proposed mutual inductances and load tracking method, including the maximum efficiency control, constant voltage control, and constant current control. Note that the proposed method is only based on measurements at the TX side, and no communication channels between the TX and the RX side are required. This property greatly enhances the flexibility and practicability of the controls.

*Application 1: (Maximum Efficiency Control):* This section verifies the maximum efficiency control based on the estimated mutual inductances. The load  $R$  is set as 25  $\Omega$ , and RX is at position 1 ( $M_1 = 14.6 \mu\text{H}$  and  $M_2 = 14.1 \mu\text{H}$ ). The initial dc voltage inputs are set as  $V_{d1} = V_{d2} = 44.8 \text{ V}$  to make sure that the measured dc voltage output  $V_{out} = 24 \text{ V}$ . In this case, the output power is fixed as  $P_{out} = V_{out}^2/R = 23.04 \text{ W}$ . With the estimated  $M_1$  and  $M_2$  according to the proposed method, the calculated coupling coefficients  $k_1$  and  $k_2$  are 0.25 and 0.24, respectively.

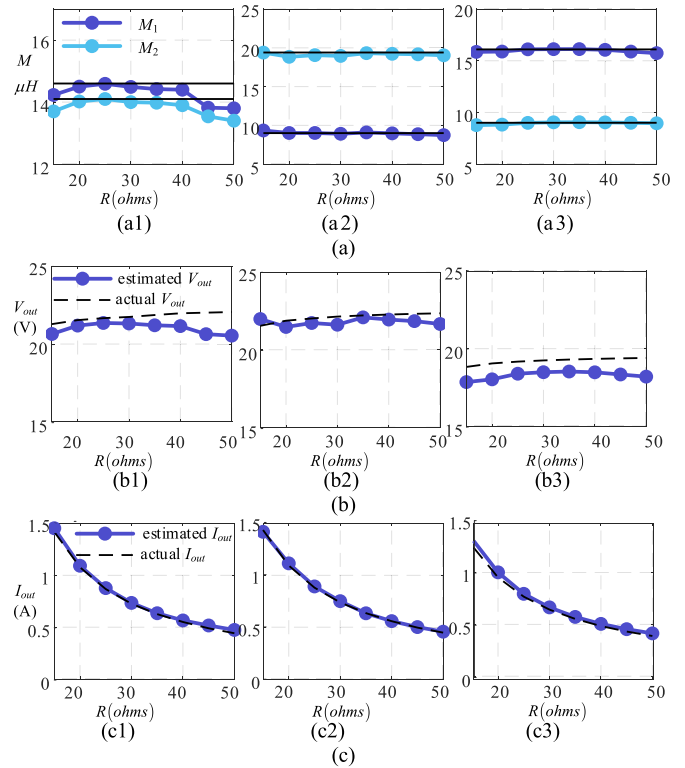


Fig. 11. Estimation results, various mutual inductances. (a) Estimation results of mutual inductances, different  $M$  and  $R$ . (a.1) Position 1. (a.2) Position 2. (a.3) Position 3. (b) Estimation results of output voltage, different  $M$  and  $R$ . (b.1) Position 1. (b.2) Position 2. (b.3) Position 3. (c) Estimation results of output current, different  $M$  and  $R$ . (c.1) Position 1. (c.2) Position 2. (c.3) Position 3.

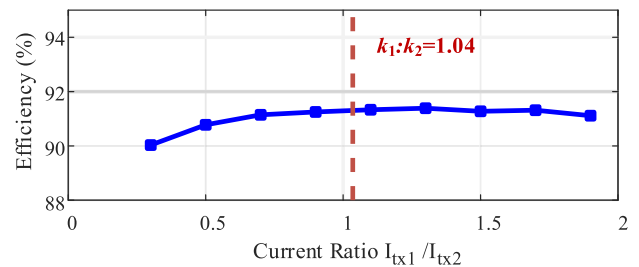


Fig. 12. Power transfer efficiency with different TX current ratios.

Next, to verify the maximum efficiency according to (21), different operating conditions with different combinations of  $\tilde{I}_{tx1}$  and  $\tilde{I}_{tx2}$  are considered (other parameters of the system remain the same). The input power from the two dc power supplies and the output power to the load can be measured by the power analyzer N4L PPA5530, and the efficiency of the system is recorded. To make those operating conditions comparable, the measured dc voltage output is fixed as  $V_{out} = 24 \text{ V}$ ; or equivalently, the measured output power is fixed as 23.04 W. Different operating conditions with different combinations of  $\tilde{I}_{tx1}$  and  $\tilde{I}_{tx2}$  are achieved by regulating the dc voltage inputs  $V_{d1}$  and  $V_{d2}$ . According to (21), the maximum efficiency should be achieved when  $\tilde{I}_{tx1}/\tilde{I}_{tx2} = k_1/k_2 = 1.04$  or  $V_{d1}/V_{d2} = (C_2k_1)/(C_1k_2) = 1.24$ .

Fig. 12 shows the efficiency with different ratios of TX currents  $\tilde{I}_{tx1}/\tilde{I}_{tx2}$ . The current ratio varies from 0.3 to 1.9,

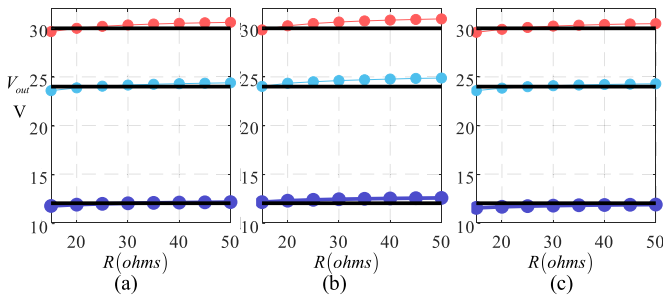


Fig. 13. Constant voltage control results, different  $M$  and  $R$ . (a) position 1. (b) position 2. (c) position 3.

with a step size of 0.2. From the figure, when the current ratio ranges from 1 to 1.3, the overall efficiency is around the maximum value of 91.7%; the efficiency decreases when the current ratio is less than 1 or is larger than 1.3. The results in this figure are consistent with the theoretical analysis where the maximum efficiency is achieved at around 1.04. Note that the maximum efficiency control of (21) only considers the efficiency of coils. The power loss of the rest of the system such as the inverter and the rectifier could also affect the measured efficiency in Fig. 12.

**Application 2 (Constant Voltage Control):** The constant voltage control is applied for the system of case 3 in Section V-B, where the target dc voltage outputs include 12, 24, and 30 V, the position of RX includes positions 1–3, and the load varies from 15 to 50  $\Omega$ . For each case with different loads at different RX positions, with the estimated voltage phasor  $\tilde{U}_1$  from the proposed method, the dc voltage output  $V_{out}$  is estimated according to (22). Afterward, with the present dc voltage inputs  $V_{d1}$  and  $V_{d2}$ , the target dc voltage inputs  $V_{d1,set}$  and  $V_{d2,set}$  can be calculated according to (23). For example, when  $V_{d1} = V_{d2} = 40$  V and  $R = 30$   $\Omega$ , with the available measurements at the transmitter side, the estimated value of  $V_{out}$  is 21.32 V. To achieve the target voltage output  $V_{out,set} = 30$  V, according to (23),  $V_{d1,set}$  and  $V_{d2,set}$  should be equal to 55.70 V. The constant voltage output independent of load is naturally satisfied due to the LCC-S topology. The results of the constant voltage control are shown in Fig. 13. The circles in red, light blue, and dark blue represent the regulated output with the target  $V_{out,set}$  as 30, 24, and 12 V, respectively. It can be observed that the measured output voltages are close to the target output voltages under different operating conditions. Also, by comparing Fig. 13 with Fig. 11(b), the importance of adopting the constant voltage control is also clearly demonstrated: the output voltage can be accurately adjusted to a user-defined value. Therefore, the effectiveness of the constant voltage control based on the estimated states is validated.

**Application 3 (Constant Current Control):** The constant current control is applied for the system of case 3 in Section V-B, where the target dc current outputs include 0.6, 0.8, and 1 A, the position of RX includes positions 1–3, and the load varies from 15 to 50  $\Omega$ . Similarly, here the dc voltage inputs are adjusted according to the estimated states for each target dc current output, RX position, and load, with  $V_{d1} = V_{d2} = 40$  V. For each case with different loads at different positions, with the estimated current phasor  $\tilde{I}_{rx1}$  and  $\tilde{I}_{rx3}$  from the proposed method, the dc current output  $I_{out}$  is estimated according to

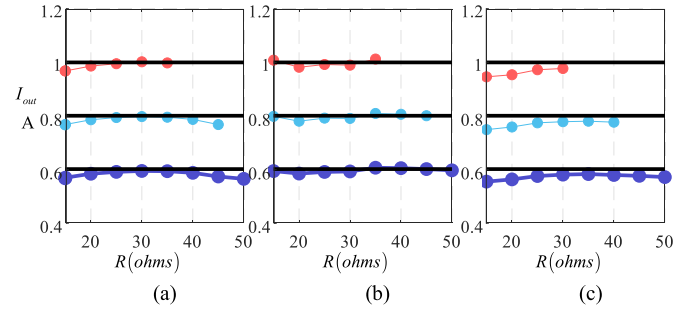


Fig. 14. Constant current control results, different  $M$  and  $R$ . (a) position 1. (b) position 2. (c) position 3.

(24). Afterward, with the present dc voltage inputs  $V_{d1}$  and  $V_{d2}$ , the target dc voltage inputs  $V_{d1,set}$  and  $V_{d2,set}$  to achieve  $I_{out,set}$  can be calculated according to (25). For example, when  $V_{d1} = V_{d2} = 40$  V and  $R = 30$   $\Omega$ , with the available measurements at the transmitter side, the estimated value of  $I_{out}$  is 0.734 A. To achieve the target current output  $I_{out,set} = 0.6$  A, according to (25),  $V_{d1,set}$  and  $V_{d2,set}$  should be equal to 32.69 V. The results of constant current control are shown in Fig. 14. The circles in red, light blue and dark blue represent the regulated output current  $I_{out}$  with the target  $I_{out,set}$  as 1, 0.8, and 0.6 A, respectively. It can be observed that the measured output currents are close to the target output currents under different operating conditions. It is worth noting that, the reason for not conducting the constant current control when  $I_{out} = 1$  A ( $R \geq 40$   $\Omega$ ) and  $I_{out} = 0.8$  A ( $R = 50$   $\Omega$ ) is the physical limitations of the voltages across the rectifier diodes: to avoid breakdown of diodes. Also, weak coupling between TX and RX will affect the accuracy of constant current control. Comparison between Figs. 11(c) and 14 also indicates the importance of constant current control: the output current becomes almost load-independent and the current value can be adjusted according to the settings. These results verify the accuracy of the proposed estimation method and the effectiveness of the constant current control.

#### D. Discussions on Combinations of Controls

In Section V-C, three control methods are presented separately as examples. During the constant voltage control and constant current control, the input voltages  $V_{d1}$  and  $V_{d2}$  are assumed to be equal to simplify the demonstrations. However, the ratios of  $V_{d1}$  and  $V_{d2}$  can also be adjusted to achieve maximum efficiency control. In this case, combinations of controls can also be achieved.

For example, to achieve maximum efficiency and constant current output at the same time, the control includes three steps. First, with example input voltages, the estimation procedure can identify the mutual inductances  $M_1$  and  $M_2$ , and the optimal ratio between  $V_{d1}$  and  $V_{d2}$  can be calculated according to (21), to ensure maximum efficiency. Second,  $V_{d1}$  and  $V_{d2}$  are adjusted to meet the optimal ratio, and the system states are estimated again to calculate  $I_{out}$  according to (24). Third, the values of  $V_{d1,set}$  and  $V_{d2,set}$  can be calculated according to (25), and the input voltages are adjusted. This control procedure can ensure maximum efficiency and constant output current at the same time. The experimental results are similar as those in Section V-C.

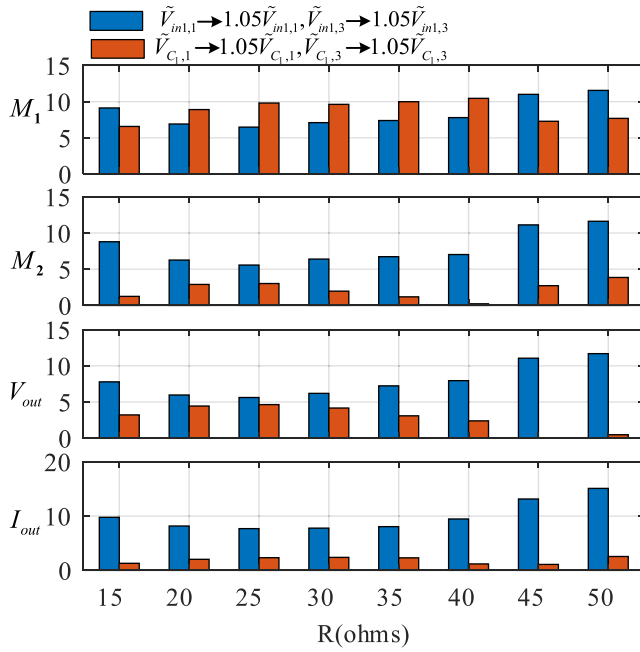


Fig. 15. Estimation error in percentage (%) of mutual inductances and outputs, with measurement error.

## VI. DISCUSSION

This section makes further discussions. First, the robustness of the proposed parameter identification method is examined by introducing measurement errors and parameter errors. Second, the applicability of the proposed method to multi-TX WPT systems and the practicability for load modeling are discussed. Third, the proposed method is compared with other existing parameter identification methods. Finally, the limitations of the proposed method and future work are discussed.

### A. Measurement Error

In this section, the 5% measurement error is added to the measurement phasors to study the effect of measurement errors on the parameter identification accuracy, including two cases for TX1. Case 1 adds 5% measurement error to phasors of  $v_{in1,1}(t)$ , where  $\tilde{V}_{in1,1}$  becomes  $1.05\tilde{V}_{in1,1}$  and  $\tilde{V}_{in1,3}$  becomes  $1.05\tilde{V}_{in1,3}$ . Case 2 adds 5% measurement error to phasors of  $v_{C1}(t)$ , where  $\tilde{V}_{C1,1}$  becomes  $1.05\tilde{V}_{C1,1}$  and  $\tilde{V}_{C1,3}$  becomes  $1.05\tilde{V}_{C1,3}$ . Here, the system settings are the same as the case 2 in Section V-B, where the RX is at position 1 and  $R$  ranges from 15 to 50  $\Omega$  with an interval of 5  $\Omega$ . The estimation errors (in percentage) of states in the two cases with 5% measurements error are shown in Fig. 15.

The result shown in Fig. 15 indicates that the maximum absolute estimation error for  $M_1$ ,  $M_2$ ,  $V_{out}$ , and  $I_{out}$  is around 10% for both case 1 and case 2. One can also observe that the measurement error of  $v_{C1}(t)$  is less influential than that of  $v_{in1,1}(t)$ , especially for the estimation of variables  $M_2$ ,  $V_{out}$ , and  $I_{out}$ .

### B. Parameter Error

Actual parameters of components such as capacitances in WPT systems could deviate from their nominal values. Here,

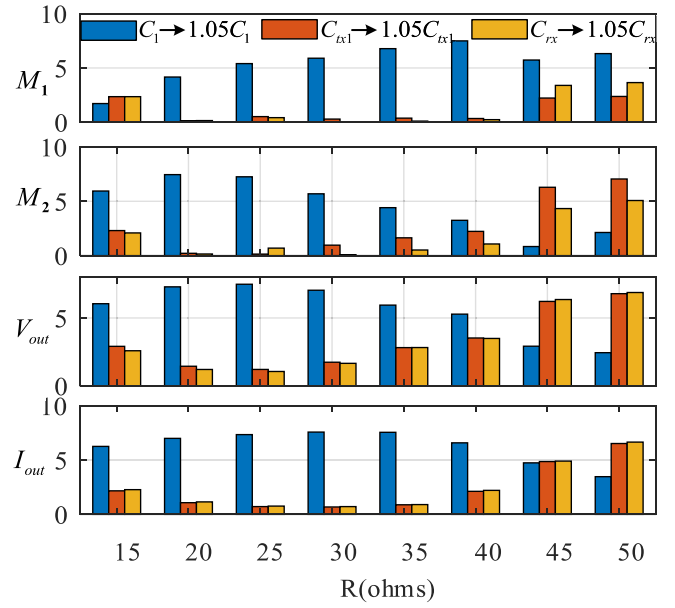


Fig. 16. Estimation error in percentage (%) of mutual inductances and outputs, with parameter error.

three cases with 5% parameter error are studied. In cases 1–3, the nominal values of  $C_1$ ,  $C_{tx1}$ , and  $C_{tx}$  in model (18) change to 1.05 times of their actual values, respectively. The actual values of the capacitances remain unchanged. The estimation error (in percentage) of states in the three cases with 5% parameters error are shown in Fig. 16. The maximum absolute estimation errors for  $M_1$ ,  $M_2$ ,  $V_{out}$ , and  $I_{out}$  is around 8% for all three cases. The results show that the parameter error of  $C_1$  has the largest impact on the estimation accuracy. Also, the impact of  $C_{tx1}$  and  $C_{tx}$  increases with lighter loads (larger value of  $R$ ).

### C. Applicability to Multi-TX WPT Systems

This article validates the proposed mutual inductances and load identification method in 2TX–1RX WPT systems. In fact, the parameter identification method can be similarly applied to multi-TX–1RX WPT systems with a similar modeling and parameter estimation procedure as in Sections II and III. First, the transmitter side model of the multi-TX WPT system includes  $m$  complex equations (each equation corresponds to each coil), where  $m$  is the number of TX coils. The format is similar to the model in (1), where  $m = 2$  in (1). Then, the receiver side model of multi-TX WPT systems is the same as the equivalent square wave source model in (10). The additional equation describing the relationship between the  $n$ th harmonic component magnitude  $U_n$  and the fundamental component magnitude  $U_1$  is the same as (13). Here similarly, the first- and third-harmonic components can be utilized to build the overall model. Finally, combine the transmitter side model ( $4m$  real equations), the receiver side model (four real equations), and the additional equation (one real equation), there will be  $(4m + 5)$  real equations. With the iteration procedure in (20), the parameters can be solved.

To demonstrate the applicability of the parameter identification method to multi-TX–1RX WPT systems, here the

TABLE II  
PARAMETERS OF MULTI-TX WPT SYSTEM

$M_1 = 14.6 \mu\text{H}, M_2 = 14.1 \mu\text{H}, M_3 = 9 \mu\text{H}, M_4 = 9 \mu\text{H}$
$M_{12} = M_{23} = M_{34} = 2 \mu\text{H}, M_{13} = M_{24} = 2 \mu\text{H}, M_{14} = 2 \mu\text{H}$
$L_3 = 25.53 \mu\text{H}, C_3 = 110 \text{ nF}, L_{r3} = 58.76 \mu\text{H}, C_{r3} = 71 \text{ nF}, r_{r3} = 0.150 \Omega$
$L_4 = 25.53 \mu\text{H}, C_4 = 110 \text{ nF}, L_{r4} = 58.76 \mu\text{H}, C_{r4} = 71 \text{ nF}, r_{r4} = 0.150 \Omega$

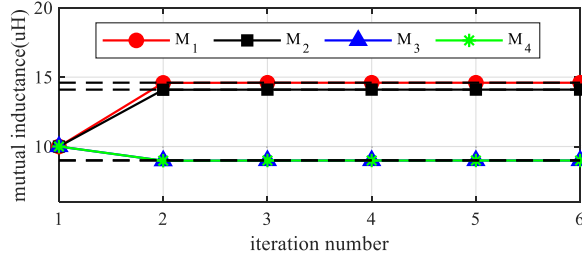


Fig. 17. Estimation results of mutual inductances, 4TX-1RX.

simulation results of a 4TX-1RX WPT system are shown as an example. The parameter settings are shown in Table II. The other settings are the same as those of case 1. Note that here the mutual inductances among TX coils are also added to cover general scenarios.

For the 4TX-1RX WPT system, the estimation results of mutual inductances ( $M_1$ ,  $M_2$ ,  $M_3$ , and  $M_4$ ) between the transmitters and the receiver are shown in Fig. 17. The estimated outputs are  $V_{\text{out}} = 38.215 \text{ V}$  and  $I_{\text{out}} = 1.275 \text{ A}$ , while the actual outputs are  $V_{\text{out}} = 38.225 \text{ V}$  and  $I_{\text{out}} = 1.274 \text{ A}$ . Estimated mutual inductances among the TX coils are  $M_{12} = 2.14 \mu\text{H}$ ,  $M_{13} = 2.02 \mu\text{H}$ ,  $M_{23} = 2.03 \mu\text{H}$ ,  $M_{14} = 2.02 \mu\text{H}$ ,  $M_{24} = 2.03 \mu\text{H}$ , and  $M_{34} = 2.06 \mu\text{H}$ . The estimation errors of voltage/current outputs and  $M_1$ - $M_4$  are smaller than 1%.

The above results demonstrate the applicability of the proposed method for multi-TX-1RX systems. However, there are other issues to be considered in practice. First, when the number of TX coils increases significantly, the number of mutual inductances among transmitters will also increase significantly. In those cases, the number of unknown mutual inductances among transmitters can be minimized by observing the following facts: 1) the mutual inductance could be neglected if two transmitters are far from each other and 2) many mutual inductances are identical from the symmetry of the coil arrangements. Second, the above parameter identification idea can be potentially extended to 1TX-multi-RX and multi-TX-multi-RX WPT systems. However, for 1TX-multi-RX and multi-TX-multi-RX WPT systems, the number of states further increases while the measurements could be limited. As a result, for each scenario, it is still necessary to strictly verify whether the redundancy is adequate to identify all the parameters of interest at the same time. Those issues should still be carefully investigated in the future.

#### D. Comparison to Existing Methods

Existing methods usually require techniques such as communication from receiver, auxiliary circuit, off-resonant frequency operation, and frequency sweeping. Some methods are designed to estimate only mutual inductances and

TABLE III  
COMPARISON TO OTHER PARAMETER IDENTIFICATION METHODS

Method	Resonant frequency operation	No frequency sweeping	No auxiliary circuit	No communication from receiver	Identify M & load	Multi-TX/RX
Ref						
[11]	√	√	√	×	×	×
[12-14,23]	√	√	√	√	×	×
[16-17]	√	√	×	√	√	×
[19]	×	√	√	√	√	×
[22]	√	×	√	√	√	√
[26, 28]	√	√	√	×	×	√
<b>Proposed</b>	√	√	√	√	√	√

assume known values of loads. Also, some methods are designed for 1TX-1RX WPT systems instead of multicoil WPT systems. Instead, the proposed method in this article can estimate mutual inductances and load at the same time, is compatible with resonant frequency operation, and the hardware cost/implementation complexity is minimized. The comparison between the proposed method and the existing methods is summarized in Table III.

#### E. Practicability for Load Modeling

In this article, the load part of the WPT system includes the rectifier, the capacitor  $C_0$  and the load  $R$ , where the load  $R$  is a pure resistor. In practice, besides constant resistance (CR) load, there are also constant voltage (CV), constant current, and constant power (CP) loads. Regardless of the load type, since the system is with dc voltage and current outputs, the load can always be equivalent to a resistor  $R$  at one operating point, and consideration of the equivalent inductance and capacitance within the load is not necessary. Utilizing the pure resistive load model is also widely accepted in the literature [11], [12], [13], [14], [15], [16], [17], [18], [19], [20], [21], [22], [23], [24], [26], [27], [28], [29], [30].

Indeed, during CV or CP load condition, the equivalent resistor  $R$  will vary at different operating points of the system. In this article, the proposed method can accurately estimate the output voltage and current during various load conditions. For example, case 2 in Section V-B can be equivalently seen as the CV load condition, where the output voltage, output current, and equivalent load resistor can still be accurately estimated. Therefore, this article adopts the pure resistive load model.

#### F. Limitations and Future Work

For simplicity, this article adopts an oscilloscope for data acquisition and MATLAB for algorithm implementation. According to the computational burden analysis in Section V, although the proposed method is an iterative method, it can still be potentially implemented in other platforms such as DSP or FPGA. Also, to further reduce the algorithm complexity and avoid the risks of divergence, analytical instead of iterative solutions of parameters are valuable and will be studied in the future.

In addition, from Sections VI-A and VI-B, one can observe that the measurement error and parameter error will affect the parameter identification accuracy to some extent. To minimize

measurement errors, advanced filtering and amplification circuits could be designed [42]. To minimize parameter errors, one can conduct parameter calibration for the WPT system before operation or propose methods that can estimate capacitor parameters and the mutual inductances/loads at the same time. Moreover, other formulations of parameter identification approaches that show more robustness toward measurement/parameter errors are attractive.

Finally, the proposed parameter identification method is derived based on steady-state operation of the system and is verified during steady state. During fast dynamics such as abrupt changes of loads or mutual inductances, the correctness of the steady-state assumption depends on the time constant of those dynamics and the requirement of time resolution of the parameter identification approach. Parameter identification methods that can track fast dynamics of parameters may still need further investigation in the future.

## VII. CONCLUSION

This article proposes a parameter identification method to identify the mutual inductances and load for 2TX–1RX LCC-S WPT systems. The method first builds a model to describe the physical laws of the transmitter and receiver sides of the WPT system, with consideration of the fundamental frequency and third harmonics of the system. This article rigorously derives the reason for parameter dependency (infinite solutions of parameters) for the equivalent resistor load modeling at the resonant frequency and presents a harmonic-based modeling method to ensure unique solutions of mutual inductances and load. After modeling the system, a state estimation method is applied to solve the unknown states, including the mutual inductances and load information. With the estimated parameters, maximum efficiency control and constant output voltage/current controls can be implemented. The proposed method only requires transmitter-side voltage measurements without any information from the receiver side and has no restrictions on the operating frequency of the system (including the resonant frequency). Hardware experimental results verify the effectiveness of the proposed parameter tracking method and control applications.

## REFERENCES

- [1] S. C. Tang, T. L. T. Lun, Z. Guo, K.-W. Kwok, and N. J. McDannold, "Intermediate range wireless power transfer with segmented coil transmitters for implantable heart pumps," *IEEE Trans. Power Electron.*, vol. 32, no. 5, pp. 3844–3857, May 2017.
- [2] G. A. Covic, J. T. Boys, M. L. G. Kissin, and H. G. Lu, "A three-phase inductive power transfer system for roadway-powered vehicles," *IEEE Trans. Ind. Electron.*, vol. 54, no. 6, pp. 3370–3378, Dec. 2007.
- [3] V.-B. Vu, D.-H. Tran, and W. Choi, "Implementation of the constant current and constant voltage charge of inductive power transfer systems with the double-sided LCC compensation topology for electric vehicle battery charge applications," *IEEE Trans. Power Electron.*, vol. 33, no. 9, pp. 7398–7410, Sep. 2018.
- [4] M. Fu, H. Yin, M. Liu, and C. Ma, "Loading and power control for a high-efficiency class E PA-driven megahertz WPT system," *IEEE Trans. Ind. Electron.*, vol. 63, no. 11, pp. 6867–6876, Nov. 2016.
- [5] C. Xiao, D. Cheng, and K. Wei, "An LCC-C compensated wireless charging system for implantable cardiac pacemakers: Theory, experiment, and safety evaluation," *IEEE Trans. Power Electron.*, vol. 33, no. 6, pp. 4894–4905, Jun. 2018.
- [6] J. P. W. Chow, N. Chen, H. S. H. Chung, and L. L. H. Chan, "An investigation into the use of orthogonal winding in loosely coupled link for improving power transfer efficiency under coil misalignment," *IEEE Trans. Power Electron.*, vol. 30, no. 10, pp. 5632–5649, Oct. 2015.
- [7] Y. Guo, Y. Zhang, W. Zhang, and L. Wang, "Battery parameter identification based on wireless power transfer system with rectifier load," *IEEE Trans. Ind. Electron.*, vol. 68, no. 8, pp. 6893–6904, Aug. 2021.
- [8] W. Zhong and S. Y. R. Hui, "Maximum energy efficiency operation of series-series resonant wireless power transfer systems using on-off keying modulation," *IEEE Trans. Power Electron.*, vol. 33, no. 4, pp. 3595–3603, Apr. 2018.
- [9] Z. Huang, S.-C. Wong, and C. K. Tse, "Control design for optimizing efficiency in inductive power transfer systems," *IEEE Trans. Power Electron.*, vol. 33, no. 5, pp. 4523–4534, May 2018.
- [10] Z. Li, K. Song, J. Jiang, and C. Zhu, "Constant current charging and maximum efficiency tracking control scheme for supercapacitor wireless charging," *IEEE Trans. Power Electron.*, vol. 33, no. 10, pp. 9088–9100, Oct. 2018.
- [11] X. Dai, X. Li, Y. Li, and A. P. Hu, "Maximum efficiency tracking for wireless power transfer systems with dynamic coupling coefficient estimation," *IEEE Trans. Power Electron.*, vol. 33, no. 6, pp. 5005–5015, Jun. 2018.
- [12] V. Jiwariyavej, T. Imura, and Y. Hori, "Coupling coefficients estimation of wireless power transfer system via magnetic resonance coupling using information from either side of the system," *IEEE J. Emerg. Sel. Topics Power Electron.*, vol. 3, no. 1, pp. 191–200, Mar. 2015.
- [13] K. Yue, Y. Liu, P. Zhao, B. Xue, and R. He, "Time domain coupling coefficient estimation using transmitter-side information in wireless power transfer system," in *Proc. 45th Annu. Conf. IEEE Ind. Electron. Soc.*, vol. 1, Oct. 2019, pp. 4189–4194.
- [14] J. Hu, J. Zhao, and C. Cui, "A wide charging range wireless power transfer control system with harmonic current to estimate the coupling coefficient," *IEEE Trans. Power Electron.*, vol. 36, no. 5, pp. 5082–5094, May 2021.
- [15] Y. Yang, S. C. Tan, and S. Y. R. Hui, "Fast hardware approach to determining mutual coupling of series-series-compensated wireless power transfer systems with active rectifiers," *IEEE Trans. Power Electron.*, vol. 35, no. 10, pp. 11026–11038, Oct. 2020.
- [16] X. Sheng and L. Shi, "Mutual inductance and load identification method for inductively coupled power transfer system based on auxiliary inverter," *IEEE Trans. Veh. Technol.*, vol. 69, no. 2, pp. 1533–1541, Feb. 2020.
- [17] Y.-G. Su, H.-Y. Zhang, Z.-H. Wang, A. P. Hu, L. Chen, and Y. Sun, "Steady-state load identification method of inductive power transfer system based on switching capacitors," *IEEE Trans. Power Electron.*, vol. 30, no. 11, pp. 6349–6355, Nov. 2015.
- [18] Y.-G. Su, L. Chen, X.-Y. Wu, A. P. Hu, C.-S. Tang, and X. Dai, "Load and mutual inductance identification from the primary side of inductive power transfer system with parallel-tuned secondary power pickup," *IEEE Trans. Power Electron.*, vol. 33, no. 11, pp. 9952–9962, Nov. 2018.
- [19] J. Yin, D. Lin, T. Parisini, and S. Y. Hui, "Front-end monitoring of the mutual inductance and load resistance in a series-series compensated wireless power transfer system," *IEEE Trans. Power Electron.*, vol. 31, no. 10, pp. 7339–7352, Oct. 2016.
- [20] J. Liu, G. Wang, G. Xu, J. Peng, and H. Jiang, "A parameter identification approach with primary-side measurement for DC–DC wireless-power-transfer converters with different resonant tank topologies," *IEEE Trans. Transport. Electrification.*, vol. 7, no. 3, pp. 1219–1235, Sep. 2021.
- [21] R. Dai, W. Zhou, Y. Chen, Z. Zhu, and R. Mai, "Pulse density modulation based mutual inductance and load resistance identification method for wireless power transfer system," *IEEE Trans. Power Electron.*, vol. 37, no. 8, pp. 9933–9943, Aug. 2022.
- [22] Y. Yang, S.-C. Tan, and S. Y. R. Hui, "Front-end parameter monitoring method based on two-layer adaptive differential evolution for SS-compensated wireless power transfer systems," *IEEE Trans. Ind. Informat.*, vol. 15, no. 11, pp. 6101–6113, Nov. 2019.
- [23] J. P. Chow, H. S. Chung, and C.-S. Cheng, "Use of transmitter-side electrical information to estimate mutual inductance and regulate receiver-side power in wireless inductive link," *IEEE Trans. Power Electron.*, vol. 31, no. 9, pp. 6079–6091, Sep. 2016.
- [24] B. H. Choi, E. S. Lee, Y. H. Sohn, G. C. Jang, and C. T. Rim, "Six degrees of freedom mobile inductive power transfer by crossed dipole Tx and Rx coils," *IEEE Trans. Power Electron.*, vol. 31, no. 4, pp. 3252–3272, Apr. 2016.

- [25] S. Huh and D. Ahn, "Two-transmitter wireless power transfer with optimal activation and current selection of transmitters," *IEEE Trans. Power Electron.*, vol. 33, no. 6, pp. 4957–4967, Jun. 2018.
- [26] D.-H. Kim, S. Kim, S.-W. Kim, J. Moon, I. Cho, and D. Ahn, "Coupling extraction and maximum efficiency tracking for multiple concurrent transmitters in dynamic wireless charging," *IEEE Trans. Power Electron.*, vol. 35, no. 8, pp. 7853–7862, Aug. 2020.
- [27] D.-H. Kim and D. Ahn, "Maximum efficiency point tracking for multiple-transmitter wireless power transfer," *IEEE Trans. Power Electron.*, vol. 35, no. 11, pp. 11391–11400, Nov. 2020.
- [28] X. Dai, J. Jiang, Z. Xu, and Y. Li, "Cooperative control for multi-excitation units WPT system with multiple coupling parameter identification and area adaptation," *IEEE Access*, vol. 8, pp. 38728–38741, 2020.
- [29] X. Dai, J.-C. Jiang, and J.-Q. Wu, "Charging area determining and power enhancement method for multiexcitation unit configuration of wirelessly dynamic charging EV system," *IEEE Trans. Ind. Electron.*, vol. 66, no. 5, pp. 4086–4096, May 2019.
- [30] S. Li, L. Wang, Y. Guo, and Z. Liu, "Flexible energy-transfer control of dynamic wireless power transfer system based on estimation of load and mutual inductance," *IEEE Trans. Ind. Appl.*, vol. 58, no. 1, pp. 1157–1167, Jan. 2022.
- [31] Q. Wang, G. Wang, N. Zhao, G. Zhang, Q. Cui, and D. Xu, "An impedance model-based multiparameter identification method of PMSM for both offline and online conditions," *IEEE Trans. Power Electron.*, vol. 36, no. 1, pp. 727–738, Jan. 2021.
- [32] Q. Wang, G. Wang, S. Liu, G. Zhang, and D. Xu, "An inverter-nonlinear-immune offline inductance identification method for PMSM drives based on equivalent impedance model," *IEEE Trans. Power Electron.*, vol. 37, no. 6, pp. 7100–7112, Jun. 2022.
- [33] G. Zhang, G. Wang, D. Xu, and N. Zhao, "ADALINE-network-based PLL for position sensorless interior permanent magnet synchronous motor drives," *IEEE Trans. Power Electron.*, vol. 31, no. 2, pp. 1450–1460, Feb. 2016.
- [34] D. Díaz Reigosa, D. Fernandez, Z.-Q. Zhu, and F. Briz, "PMSM magnetization state estimation based on stator-reflected PM resistance using high-frequency signal injection," *IEEE Trans. Ind. Appl.*, vol. 51, no. 5, pp. 3800–3810, Sep./Oct. 2015.
- [35] S. A. Odhano, P. Pescetto, H. A. A. Awan, M. Hinkkanen, G. Pellegrino, and R. Bojoi, "Parameter identification and self-commissioning in AC motor drives: A technology status review," *IEEE Trans. Power Electron.*, vol. 34, no. 4, pp. 3603–3614, Apr. 2019.
- [36] G. Fusco, A. Losi, and M. Russo, "Constrained least squares methods for parameter tracking of power system steady-state equivalent circuits," *IEEE Trans. Power Del.*, vol. 15, no. 3, pp. 1073–1080, Jul. 2000.
- [37] A. A. Girgis, W. B. Chang, and E. B. Makram, "A digital recursive measurement scheme for online tracking of power system harmonics," *IEEE Trans. Power Del.*, vol. 6, no. 3, pp. 1153–1160, Jul. 1991.
- [38] C.-I. Chen and Y.-C. Chen, "Comparative study of harmonic and inter-harmonic estimation methods for stationary and time-varying signals," *IEEE Trans. Ind. Electron.*, vol. 61, no. 1, pp. 397–404, Jan. 2014.
- [39] M. Karimi-Ghartemani and M. R. Iravani, "Measurement of harmonics/inter-harmonics of time-varying frequencies," *IEEE Trans. Power Del.*, vol. 20, no. 1, pp. 23–31, Jan. 2005.
- [40] A. Zaheer, G. A. Covic, and D. Kacprzak, "A bipolar pad in a 10-kHz 300-W distributed IPT system for AGV applications," *IEEE Trans. Ind. Electron.*, vol. 61, no. 7, pp. 3288–3301, Jul. 2014.
- [41] Y. Liu et al., "Dynamic state estimation for power system control and protection," *IEEE Trans. Power Syst.*, vol. 36, no. 6, pp. 5909–5921, Nov. 2021.
- [42] Z. Cui, N. Cui, C. Wang, C. Li, and C. Zhang, "A robust online parameter identification method for lithium-ion battery model under asynchronous sampling and noise interference," *IEEE Trans. Ind. Electron.*, vol. 68, no. 10, pp. 9550–9560, Oct. 2021.
- [43] Y. Li, R. Mai, L. Lu, T. Lin, Y. Liu, and Z. He, "Analysis and transmitter currents decomposition based control for multiple overlapped transmitters based WPT systems considering cross couplings," *IEEE Trans. Power Electron.*, vol. 33, no. 2, pp. 1829–1842, Feb. 2018.
- [44] J. M. Miller, P. T. Jones, J.-M. Li, and O. C. Onar, "ORNL experience and challenges facing dynamic wireless power charging of EV's," *IEEE Circuits Syst. Mag.*, vol. 15, no. 2, pp. 40–53, 2nd Quart., 2015.
- [45] G. Bouattour, H. Ben Jemaa Derbel, and O. Kanoun, "Multi-parallel sending coils for movable receivers in inductive charging systems," in *Proc. 16th Int. Multi-Conf. Syst., Signals Devices (SSD)*, Istanbul, Turkey, Mar. 2019, pp. 758–762.
- [46] J. Feng, Q. Li, F. C. Lee, and M. Fu, "LCCL-LC resonant converter and its soft switching realization for omnidirectional wireless power transfer systems," *IEEE Trans. Power Electron.*, vol. 36, no. 4, pp. 3828–3839, Apr. 2021.
- [47] W. M. Ng, C. Zhang, D. Lin, and S. Y. Ron Hui, "Two- and three-dimensional omnidirectional wireless power transfer," *IEEE Trans. Power Electron.*, vol. 29, no. 9, pp. 4470–4474, Sep. 2014.
- [48] J. Feng, Q. Li, and F. C. Lee, "Coil and circuit design of omnidirectional wireless power transfer system for portable device application," in *Proc. IEEE Energy Convers. Congr. Expo. (ECCE)*, Portland, OR, USA, Sep. 2018, pp. 914–920.



**Kang Yue** (Graduate Student Member, IEEE) received the B.S. degree in electrical engineering and its automation from the Hefei University of Technology, Hefei, China, in 2017, and the Ph.D. degree in electrical and electronic engineering from ShanghaiTech University, Shanghai, China, and the University of the Chinese Academy of Sciences, Beijing, China, in 2023.

During her Ph.D. study, her research focus on health monitoring and parameter identification of power electronic systems. She is currently an Engineer with the China Electric Power Research Institute, SGCC, Beijing.



**Yu Liu** (Senior Member, IEEE) received the B.S. and M.S. degrees in electrical power engineering from Shanghai Jiao Tong University, Shanghai, China, in 2011 and 2013, respectively, and the Ph.D. degree in electrical and computer engineering from the Georgia Institute of Technology, Atlanta, GA, USA, in 2017.

He is currently a Tenured Associate Professor with the School of Information Science and Technology, ShanghaiTech University, Shanghai. He has authored or coauthored three book chapters and more than 110 technical articles. His research interests include modeling, protection, fault location, and state/parameter estimation of power systems, and power electronic systems.

Dr. Liu was a recipient of the 2023 IEEE PES Outstanding Working Group for Outstanding Technical Report Award and the Shanghai Eastern Scholar Professorship and Shanghai Pujiang Scholar. He serves as an Associate Editor for the *IET Renewable Power Generation (RPG)* and a Guest Editor for the *Journal of Modern Power Systems and Clean Energy (MPCE)*.



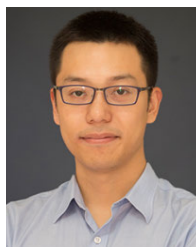
**Xinguo Zhang** (Graduate Student Member, IEEE) received the B.S. degree in electrical engineering and automation from Fuzhou University, Fuzhou, China, in 2019. He is currently pursuing the Ph.D. degree in power electronics with the School of Information Science and Technology, ShanghaiTech University, Shanghai, China.

His current research interests include fault diagnosis and condition monitoring of power electronic circuits.



**Minfan Fu** (Senior Member, IEEE) received the B.S. degree in electrical and computer engineering from the University of Michigan, Ann Arbor, MI, USA, in 2010, the M.S. degree in electrical and computer engineering from the Shanghai Jiao Tong University Joint Institute, Shanghai, China, in 2013, and the Ph.D. degree from Shanghai Jiao Tong University, Shanghai, in 2016.

From 2016 to 2018, he held a post-doctoral position at the Center for Power Electronics Systems (CPES), Virginia Polytechnic Institute and State University, Blacksburg, VA, USA. He is currently an Assistant Professor with the School of Information Science and Technology, ShanghaiTech University, Shanghai. His research interests include wireless power transfer (WPT), high-frequency power conversion, high-frequency magnetic design, and application of wide bandgap devices.



**Haoyu Wang** (Senior Member, IEEE) received the bachelor's degree (Hons.) in electrical engineering from Zhejiang University, Hangzhou, China, in 2009, and the Ph.D. degree in electrical engineering from the University of Maryland at College Park, College Park, MD, USA, in 2014.

In September 2014, he joined the School of Information Science and Technology, ShanghaiTech University, Shanghai, China, where he is currently a tenured Associate Professor. His research interests include power electronics, plug-in electric and hybrid electric vehicles, the applications of wide bandgap semiconductors, renewable energy harvesting, and power management integrated circuits.

Dr. Wang is an Associate Editor of *IEEE TRANSACTIONS ON INDUSTRIAL ELECTRONICS*, *IEEE TRANSACTIONS ON TRANSPORTATION ELECTRIFICATION*, and *CPSS Transactions on Power Electronics and Applications*.



**Junrui Liang** (Senior Member, IEEE) received the B.E. and M.E. degrees in instrumentation engineering from Shanghai Jiao Tong University, Shanghai, China, in 2004 and 2007, respectively, and the Ph.D. degree in mechanical and automation engineering from The Chinese University Hong Kong, Hong Kong, China, in 2010.

He is currently an Associate Professor with the School of Information Science and Technology, ShanghaiTech University, Shanghai. His research interests include energy conversion and power conditioning circuits, kinetic energy harvesting and vibration suppression, the Internet-of-Things (IoT) devices, and mechatronics.

Dr. Liang is an Associate Editor of *IET Circuits, Devices and Systems* and the General Chair of the Second International Conference on Vibration and Energy Harvesting Applications (VEH) in 2019.